

Chapter 7

NV Center Physics for Quantum Field Imaging

The Quantum Transducer: From Physical Fields to Optical Signals

This chapter establishes the nitrogen-vacancy (NV) center as the quantum transducer that converts physical fields into measurable optical signals. We develop the complete spin Hamiltonian from first principles, derive the ODMR mechanism, and establish fundamental sensitivity limits.

Central Question: How does NV center physics determine η_q in Q_{FOM} , and what material/physics factors limit achievable sensitivity?

Operator Focus: \mathbf{M} (quantum transduction layer of the measurement operator) Chapter 7 specifically addresses the physical transduction mechanism — the NV center — that converts field perturbations into detectable spin state changes.

Key Outputs:

- Complete NV Hamiltonian with all sensing modalities
- ODMR contrast mechanism and optimization
- Shot-noise limited sensitivity derivation
- Multi-physics capability foundations for $\Phi_{\text{multi}} > 1$
- Material quality requirements and failure modes
- Array engineering from 1D to 3D configurations
- Super-resolution techniques for nanoscale imaging

QFI Pipeline Position: $S \xrightarrow{G} F \xrightarrow{\boxed{\mathcal{M}}} D \xrightarrow{R} \hat{S}$

Abbreviated Terms

Table 7.1: Abbreviated terms used in Chapter 7.

Abbrev.	Full Term	Abbrev.	Full Term
CW	Continuous Wave	NV	Nitrogen-Vacancy
CVD	Chemical Vapor Deposition	ODMR	Optically Detected Magnetic Resonance
ESR	Electron Spin Resonance	PL	Photoluminescence
FWHM	Full Width at Half Maximum	PSB	Phonon Sideband
GeV	Germanium-Vacancy	QFI	Quantum Field Imaging
GHz	Gigahertz	QY	Quantum Yield
HPHT	High Pressure High Temperature	SiC	Silicon Carbide
hBN	Hexagonal Boron Nitride	SiV	Silicon-Vacancy
ISC	Intersystem Crossing	SnV	Tin-Vacancy
MW	Microwave	SQL	Standard Quantum Limit
N_{NV}	NV Center Count	ZFS	Zero-Field Splitting
ZPL	Zero-Phonon Line	CSD	Charge State Depletion

Abstract

The nitrogen-vacancy (NV) center in diamond serves as the exemplar quantum sensor for Quantum Field Imaging, functioning as the critical transducer that converts physical fields (magnetic, thermal, strain, electric) into optically detectable signals. This chapter develops the complete theoretical framework for NV center physics from first principles, beginning with the diamond crystal structure and electronic configuration, then deriving the full spin Hamiltonian that governs multi-physics sensing. We establish the optically detected magnetic resonance (ODMR) mechanism that enables room-temperature quantum sensing, derive fundamental sensitivity limits from quantum projection noise, and identify the material quality factors that determine practical performance. The chapter concludes by examining engineered NV arrays from 1D to 3D configurations, super-resolution techniques including CSD, STORM-NV, and Spin-RESOLFT, and alternative color center systems (SiV, GeV, SnV) that may complement or extend NV capabilities for next-generation QFI systems. Design rules are established to guide sensor optimization for semiconductor failure analysis applications.

7.1 Introduction: Why NV Center Physics Matters for QFI

7.1.1 The Quantum Transduction Challenge

At the heart of every Quantum Field Imaging system lies a fundamental challenge: converting invisible physical fields—magnetic, thermal, strain, electric—into optical signals that cameras can detect. The NV center in diamond solves this transduction problem with remarkable elegance, providing:

- **Room-temperature operation:** Unlike superconducting sensors requiring cryogenic cooling
- **Optical readout:** Single-photon sensitivity with standard detectors
- **Multi-physics capability:** Simultaneous sensitivity to B , T , σ , E fields
- **Nanoscale resolution:** Atomic-sized sensor (0.3 nm) with nm-scale localization
- **Material robustness:** Diamond’s chemical inertness and mechanical stability

7.1.2 Historical Development

The NV center’s journey from crystallographic curiosity to quantum sensor spans five decades:

Table 7.2: Historical milestones in NV center development.

Year	Milestone	Significance
1965	First observation of NV luminescence	du Preez thesis
1997	Single NV detection at room temperature	Gruber et al.
2004	ODMR-based magnetometry demonstrated	Jelezko et al.
2008	Sub-micron magnetic imaging	Balasubramanian et al.
2012	pT-level sensitivity achieved	Le Sage et al.
2015	Wide-field current imaging in ICs	Nowodzinski et al.
2020	Commercial QFI systems available	Multiple vendors

7.1.3 Pain Points in Current Quantum Sensing

Despite remarkable progress, several pain points limit NV-based QFI deployment:

1. **Throughput bottleneck:** Serial scanning limits inspection speed

2. **Sensitivity-resolution trade-off:** Higher resolution requires smaller sensor volume
3. **Depth ambiguity:** 2D measurement cannot uniquely determine 3D sources
4. **Material variability:** Diamond quality directly impacts performance
5. **Multi-physics cross-talk:** B, T, σ signals can be difficult to separate

This chapter addresses each pain point by developing the physics foundation needed for informed system design.

7.1.4 Chapter Objectives and Figure of Merit

The primary figure of merit connecting NV physics to QFI performance is the quantum sensitivity η_q :

Key Equation: Quantum Sensitivity

$$\eta_q = \frac{\pi\hbar\Gamma}{2g_e\mu_B C\sqrt{R}} \quad (7.1)$$

where Γ is the ODMR linewidth, C is the contrast, and R is the photon detection rate.

The Q_{FOM} from Chapter 1 directly incorporates η_q :

$$Q_{\text{FOM}} = \frac{\eta_q}{\eta_{\text{classical}}} \times \frac{N_{\text{parallel}}}{t_{\text{acquisition}}} \times \Phi_{\text{multi}} \quad (7.2)$$

This chapter provides the physics understanding needed to optimize η_q and enable $\Phi_{\text{multi}} > 1$ through multi-physics sensing.

7.2 Diamond Crystal Structure and NV Formation

7.2.1 The Diamond Lattice

Diamond crystallizes in the face-centered cubic (FCC) structure with two interpenetrating FCC sublattices, creating the diamond cubic structure with space group $Fd\bar{3}m$.

Definition 7.2.1 (Diamond Unit Cell). The diamond unit cell contains 8 carbon atoms with lattice constant $a = 3.567 \text{ \AA}$. Each carbon atom is tetrahedrally coordinated with four nearest neighbors at distance $d = a\sqrt{3}/4 = 1.545 \text{ \AA}$, forming sp^3 hybrid bonds.

The tetrahedral coordination creates four equivalent $\langle 111 \rangle$ crystallographic axes, which become important for NV center orientation:

$$\hat{\mathbf{n}}_1 = \frac{1}{\sqrt{3}}(1, 1, 1), \quad \hat{\mathbf{n}}_2 = \frac{1}{\sqrt{3}}(1, -1, -1), \quad \hat{\mathbf{n}}_3 = \frac{1}{\sqrt{3}}(-1, 1, -1), \quad \hat{\mathbf{n}}_4 = \frac{1}{\sqrt{3}}(-1, -1, 1) \quad (7.3)$$

7.2.2 NV Center Structure

The nitrogen-vacancy center consists of a substitutional nitrogen atom adjacent to a carbon vacancy, aligned along one of the four $\langle 111 \rangle$ axes.

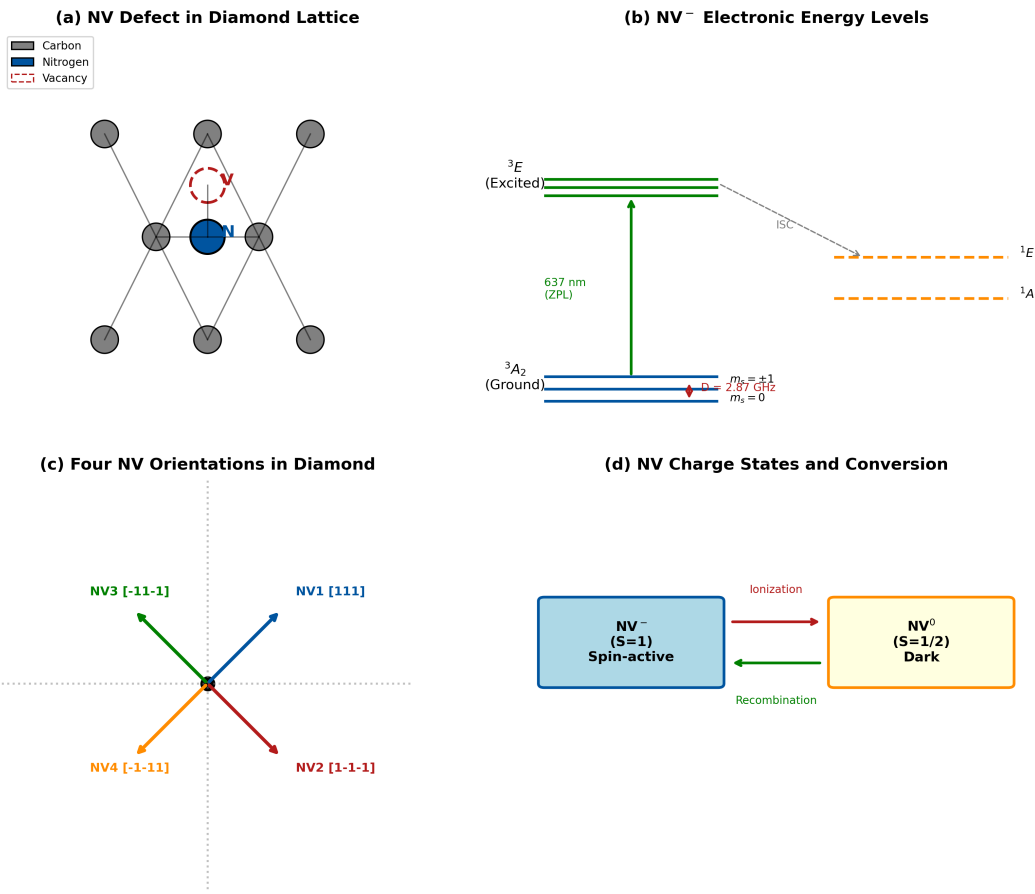
Figure 7.1: NV Center Structure and Electronic Configuration

Figure 7.1: NV center structure in diamond. (a) Crystal structure showing substitutional nitrogen (blue) adjacent to vacancy (white) along $\langle 111 \rangle$. (b) C_{3v} point group symmetry. (c) Four possible NV orientations in the diamond lattice. (d) Local electronic orbitals forming the defect states.

Figure 7.1 Interpretation:

- Panel (a) shows the atomic arrangement: three carbon atoms surround the vacancy, with nitrogen at the apex
- Panel (b) illustrates C_{3v} symmetry: three-fold rotation axis along N-V bond, three mirror planes
- Panel (c) demonstrates that any macroscopic diamond contains NV centers in all four orientations with equal probability (in unstrained material)
- Panel (d) shows the dangling bonds that combine to form the defect molecular orbitals

7.2.3 Electronic Configuration

The NV center exists in two charge states relevant for sensing:

Table 7.3: NV charge state comparison.

Property	NV ⁻	NV ⁰
Total electrons	6	5
Ground state spin	$S = 1$ (triplet)	$S = 1/2$ (doublet)
ZPL wavelength	637 nm (1.945 eV)	575 nm (2.156 eV)
Spin-dependent PL	Yes (sensing enabled)	No
ODMR observable	Yes	No

Definition 7.2.2 (NV⁻ Center). The negatively charged NV center (NV⁻) contains six electrons: three from dangling carbon bonds, two from nitrogen lone pair, and one captured from the lattice. This configuration produces a spin-1 ground state essential for magnetic sensing.

The NV⁻ charge state is required for QFI sensing. Maintaining high NV⁻ fraction ($\geq 70\%$) is a critical design consideration addressed in Section 7.7.

7.3 The Complete Spin Hamiltonian

7.3.1 Motivation: Why the Hamiltonian Matters

The NV spin Hamiltonian is the foundation for all sensing modalities. Each term in the Hamiltonian couples to a different physical quantity, enabling the multi-physics capability that distinguishes QFI from conventional imaging.

7.3.2 Ground State Spin Hamiltonian

The complete ground-state Hamiltonian for NV⁻ is:

Key Equation: NV Ground State Hamiltonian

$$\mathcal{H} = \underbrace{D_{\text{gs}} S_z^2}_{\text{ZFS}} + \underbrace{g_e \mu_B \mathbf{B} \cdot \mathbf{S}}_{\text{Zeeman}} + \underbrace{\mathbf{S} \cdot \mathbf{A} \cdot \mathbf{I}}_{\text{Hyperfine}} + \underbrace{d_{\parallel} \sigma_z S_z^2 + d_{\perp} (\sigma_x S_x + \sigma_y S_y)}_{\text{Strain/Electric}} \quad (7.4)$$

where:

- $D_{\text{gs}} = 2.87$ GHz is the zero-field splitting
- $g_e \approx 2.0028$ is the electron g-factor
- $\mu_B = 9.274 \times 10^{-24}$ J/T is the Bohr magneton
- \mathbf{A} is the hyperfine tensor
- d_{\parallel}, d_{\perp} are strain coupling coefficients

Design Rule 1: Each Hamiltonian Term Enables Sensing

Each term in Eq. 7.4 couples to a different physical quantity:

- ZFS term → Temperature sensing (via dD/dT)
- Zeeman term → Magnetic field sensing
- Strain term → Stress/strain sensing
- Electric field modifies strain term → E-field sensing

This multi-physics capability is the foundation for $\Phi_{\text{multi}} > 1$.

7.3.3 Zero-Field Splitting (ZFS)

7.3.3.1 Physical Origin

The zero-field splitting D arises from spin-spin dipolar interaction between the two unpaired electrons in the ground state. In the principal axis frame (z along N-V axis):

$$\mathcal{H}_{\text{ZFS}} = D \left(S_z^2 - \frac{S(S+1)}{3} \right) + E(S_x^2 - S_y^2) \quad (7.5)$$

For ideal C_{3v} symmetry, $E = 0$. Strain breaks this symmetry, introducing non-zero E .

At zero magnetic field, the ZFS creates the characteristic energy level structure:

- $|m_s = 0\rangle$ state at energy 0
- $|m_s = \pm 1\rangle$ states degenerate at energy $D = 2.87$ GHz

7.3.3.2 Temperature Dependence

The ZFS exhibits strong temperature dependence:

$$D(T) = D_0 + \frac{dD}{dT} \cdot (T - T_0) \quad (7.6)$$

with $dD/dT = -74.2$ kHz/K near room temperature. This enables thermometry with sensitivity:

$$\eta_T = \frac{\eta_B}{\gamma_{\text{NV}}} \cdot \left| \frac{dD}{dT} \right|^{-1} \approx 10 \text{ mK}/\sqrt{\text{Hz}} \quad (7.7)$$

Table 7.4: Temperature dependence parameters.

Parameter	Value	Temperature Range
D_0	2.8777 GHz	At 300 K
dD/dT	-74.2 kHz/K	280–350 K
d^2D/dT^2	-0.1 kHz/K ²	280–350 K

7.3.4 Zeeman Interaction

The Zeeman term describes coupling to external magnetic fields:

$$\mathcal{H}_{\text{Zeeman}} = g_e \mu_B \mathbf{B} \cdot \mathbf{S} = \gamma_{\text{NV}} (B_x S_x + B_y S_y + B_z S_z) \quad (7.8)$$

where the gyromagnetic ratio is:

$$\gamma_{\text{NV}} = \frac{g_e \mu_B}{h} = 28.025 \text{ GHz/T} = 28.025 \text{ MHz/mT} \quad (7.9)$$

For an axial field B_z along the NV axis, the $|m_s = \pm 1\rangle$ degeneracy is lifted:

$$\nu_{\pm} = D \pm \gamma_{\text{NV}} B_z \quad (7.10)$$

Design Rule 2: Magnetic Field Extraction

Extract B_z from the ODMR splitting:

$$B_z = \frac{\nu_+ - \nu_-}{2\gamma_{\text{NV}}} = \frac{\Delta\nu}{56.05 \text{ MHz/mT}} \quad (7.11)$$

7.3.5 Hyperfine Interaction

The hyperfine interaction couples electron spin to nuclear spins:

$$\mathcal{H}_{\text{HF}} = A_{\parallel} S_z I_z + A_{\perp} (S_x I_x + S_y I_y) \quad (7.12)$$

For ^{14}N (99.6% natural abundance, $I = 1$):

- $A_{\parallel} = -2.14$ MHz
- $A_{\perp} = -2.70$ MHz

This creates a characteristic three-line hyperfine structure in high-resolution ODMR, with splitting of 2.2 MHz.

For ^{13}C nuclei in the diamond lattice (1.1% natural abundance, $I = 1/2$), the hyperfine coupling depends on position and creates additional structure that can limit coherence time.

7.3.6 Strain and Electric Field Coupling

Strain breaks the C_{3v} symmetry, introducing transverse ZFS:

$$\mathcal{H}_{\text{strain}} = d_{\parallel} \sigma_z \left(S_z^2 - \frac{2}{3} \right) + d_{\perp} (\sigma_x (S_y^2 - S_x^2) + \sigma_y (S_x S_y + S_y S_x)) \quad (7.13)$$

Coupling coefficients:

- $d_{\parallel} = 5.46$ MHz/GPa (axial strain)
- $d_{\perp} = 19.63$ MHz/GPa (transverse strain)

Electric fields couple similarly through the linear Stark effect:

$$\mathcal{H}_E = d'_{\parallel} E_z S_z^2 + d'_{\perp} (E_x S_x + E_y S_y) \quad (7.14)$$

with $d'_{\perp} \approx 17$ Hz·cm/V for transverse fields.

Table 7.5: Summary of NV sensing channels from Hamiltonian terms.

Physical Field	Hamiltonian Term	Coupling Constant	Typical Sensitivity
Magnetic (B)	Zeeman	28.025 GHz/T	1 nT/ $\sqrt{\text{Hz}}$
Temperature (T)	ZFS	-74.2 kHz/K	10 mK/ $\sqrt{\text{Hz}}$
Strain (σ)	Strain	5–20 MHz/GPa	100 kPa/ $\sqrt{\text{Hz}}$
Electric (E)	Stark	17 Hz·cm/V	100 V/cm/ $\sqrt{\text{Hz}}$

7.4 Optically Detected Magnetic Resonance (ODMR)

7.4.1 Motivation: The Optical Readout Advantage

ODMR enables spin-state readout through fluorescence intensity, converting magnetic resonance signals from GHz microwave photons to visible photons detectable with standard cameras. This optical readout provides:

- Single-spin sensitivity (single photon per readout)
- Parallelizable detection (camera-based wide-field imaging)
- Room-temperature operation
- No need for cryogenic microwave amplifiers

7.4.2 Spin-Dependent Fluorescence Mechanism

The ODMR mechanism relies on spin-dependent intersystem crossing (ISC) through singlet states:

Figure 7.2: ODMR Spectroscopy Fundamentals

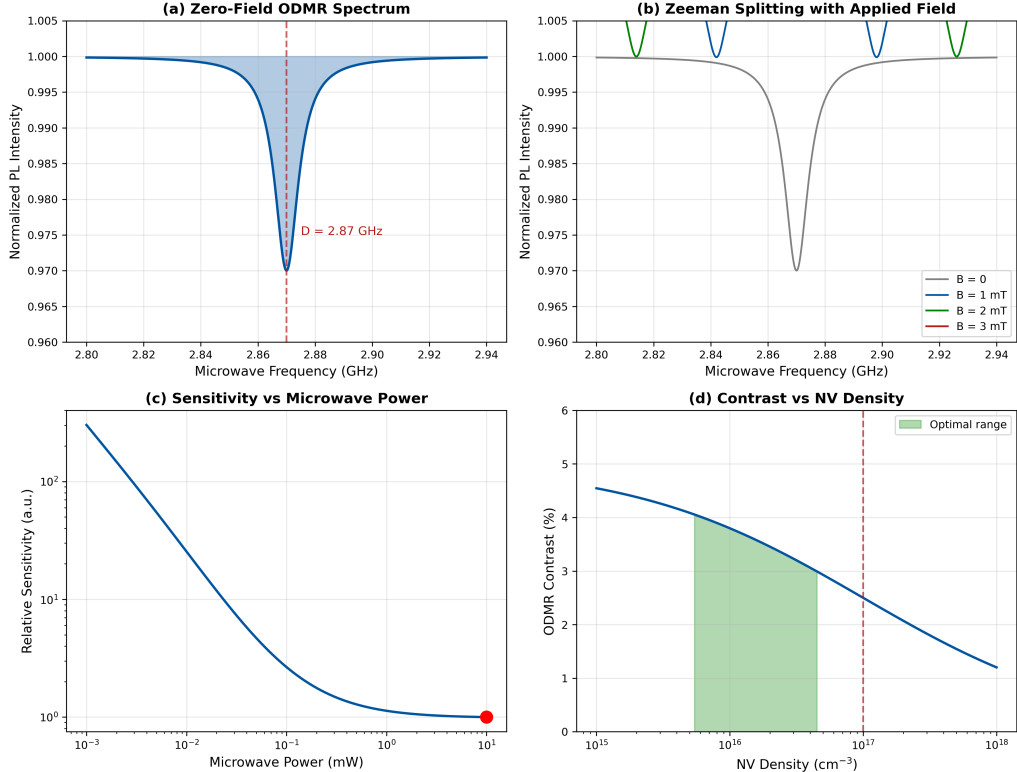


Figure 7.2: ODMR spectroscopy fundamentals. (a) Zero-field ODMR spectrum showing dip at $D = 2.87$ GHz. (b) Zeeman splitting with applied magnetic field. (c) Sensitivity optimization versus microwave power. (d) ODMR contrast dependence on NV density.

The ODMR cycle:

1. **Optical excitation:** 532 nm light pumps NV⁻ from ground 3A_2 to excited 3E
2. **Spin-conserving emission:** Most decay returns via 637 nm ZPL + PSB emission
3. **Spin-dependent ISC:** $|m_s = \pm 1\rangle$ states have higher ISC rate to singlet 1A_1
4. **Spin polarization:** Singlet decay preferentially populates $|m_s = 0\rangle$
5. **Contrast generation:** $|m_s = \pm 1\rangle$ fluorescence is dimmer due to ISC pathway

7.4.3 ODMR Contrast Derivation

The ODMR contrast C quantifies the fluorescence difference between $|m_s = 0\rangle$ and $|m_s = \pm 1\rangle$ populations:

$$C = \frac{I_0 - I_{\pm 1}}{I_0} \quad (7.15)$$

7.4.3.1 Rate Equation Model

The population dynamics are governed by:

$$\frac{d\rho_i}{dt} = -\sum_j W_{ij}\rho_i + \sum_j W_{ji}\rho_j \quad (7.16)$$

where W_{ij} are transition rates between levels i and j .

Key rates:

- $k_r = 65$ MHz: Radiative decay rate
- $k_{ISC}^0 = 0.8$ MHz: ISC rate from $m_s = 0$ excited state
- $k_{ISC}^{\pm 1} = 53$ MHz: ISC rate from $m_s = \pm 1$ excited states
- $k_S = 1.2$ MHz: Singlet decay rate

7.4.3.2 Steady-State Solution

Under continuous optical excitation, the steady-state contrast is:

$$C_0 = \frac{k_{ISC}^{\pm 1} - k_{ISC}^0}{k_r + k_{ISC}^{\pm 1}} \cdot \frac{k_S}{k_S + k_{ISC}^0} \approx 0.30 \quad (7.17)$$

Including microwave power broadening:

$$C = \frac{C_0}{1 + (\Omega_R/\Gamma)^2} \quad (7.18)$$

where Ω_R is the Rabi frequency and Γ is the intrinsic linewidth.

Design Rule 1: Optimal Microwave Power

Maximum sensitivity occurs when the Rabi frequency matches the linewidth:

$$\Omega_R^{\text{opt}} \approx \Gamma \quad (7.19)$$

Higher power increases signal but broadens the line; lower power gives narrower lines but weaker signal.

7.4.4 ODMR Linewidth and Lineshape

The ODMR lineshape is typically Lorentzian for homogeneously broadened systems:

$$\mathcal{L}(\nu - \nu_0) = \frac{1}{\pi} \frac{\Gamma/2}{(\nu - \nu_0)^2 + (\Gamma/2)^2} \quad (7.20)$$

The observed linewidth Γ has contributions:

$$\Gamma = \Gamma_{\text{intrinsic}} + \Gamma_{\text{power}} + \Gamma_{\text{inhom}} \quad (7.21)$$

Table 7.6: Linewidth contributions for different NV configurations.

Configuration	Γ_{inhom} (MHz)	Γ_{total} (MHz)	Dominant Broadening
Single NV (high purity)	< 0.1	1–3	Power broadening
Ensemble (CVD)	1–5	3–10	^{13}C hyperfine
Ensemble (HPHT)	5–20	10–30	N_s^0 bath
Nano-diamond	10–50	15–60	Surface effects

7.5 Fundamental Sensitivity Limits

7.5.1 The Sensitivity Figure of Merit

Magnetic field sensitivity η_B quantifies the minimum detectable field change per unit measurement time. Lower values indicate better sensors. The standard definition:

$$\eta_B = \delta B_{\min} \cdot \sqrt{t} \quad (7.22)$$

with units of $T/\sqrt{\text{Hz}}$ (or equivalently $T \cdot \text{s}^{1/2}$).

7.5.2 Derivation: Shot-Noise Limited Sensitivity

7.5.2.1 Step 1: Signal Definition

The ODMR signal at frequency ν near resonance ν_0 :

$$I(\nu) = I_0 [1 - C \cdot \mathcal{L}(\nu - \nu_0)] \quad (7.23)$$

A magnetic field shift δB moves the resonance:

$$\delta\nu_0 = \gamma_{\text{NV}} \cdot \delta B \quad (7.24)$$

7.5.2.2 Step 2: Maximum Slope Point

The signal change is maximized at the point of steepest slope, occurring at $\nu = \nu_0 \pm \Gamma/2$:

$$\left| \frac{\partial I}{\partial \nu} \right|_{\max} = \frac{2CI_0}{\pi\Gamma} \quad (7.25)$$

7.5.2.3 Step 3: Noise Model

For shot-noise limited detection, the photon count uncertainty in time t is:

$$\delta N = \sqrt{R \cdot t} \quad (7.26)$$

where $R = I_0/(\hbar\omega)$ is the detected photon rate.

7.5.2.4 Step 4: Minimum Detectable Field

Setting the signal change equal to the noise floor:

$$\delta I = \left| \frac{\partial I}{\partial \nu} \right| \cdot \gamma_{\text{NV}} \cdot \delta B_{\min} = \delta N = \sqrt{Rt} \quad (7.27)$$

Solving for δB_{\min} :

Key Equation: Shot-Noise Limited Sensitivity

$$\eta_B = \delta B_{\min} \sqrt{t} = \frac{\pi\hbar\Gamma}{2g_e\mu_B C \sqrt{R}} \quad (7.28)$$

Theorem 7.5.1 (Shot-Noise Limited Magnetic Sensitivity). *For an NV center with ODMR linewidth Γ , contrast C , and photon detection rate R , the shot-noise limited magnetic sensitivity is:*

$$\eta_B = \frac{\pi\hbar\Gamma}{2g_e\mu_B C \sqrt{R}} \approx \frac{1.1 \times 10^{-11}}{\sqrt{R}} \cdot \frac{\Gamma/\text{MHz}}{C} \quad [\text{T}/\sqrt{\text{Hz}}] \quad (7.29)$$

Proof. Substituting $g_e = 2.0028$, $\mu_B = 9.274 \times 10^{-24}$ J/T, and expressing Γ in MHz:

$$\eta_B = \frac{\pi \cdot (1.055 \times 10^{-34} \text{ J} \cdot \text{s}) \cdot \Gamma}{2 \cdot 2.0028 \cdot (9.274 \times 10^{-24} \text{ J/T}) \cdot C \cdot \sqrt{R}} \quad (7.30)$$

$$= \frac{\pi \cdot 1.055 \times 10^{-34}}{2 \cdot 1.858 \times 10^{-23}} \cdot \frac{\Gamma}{C\sqrt{R}} \quad (7.31)$$

$$= 8.9 \times 10^{-12} \cdot \frac{\Gamma/\text{Hz}}{C\sqrt{R}} \quad (7.32)$$

$$\approx \frac{1.1 \times 10^{-11}}{\sqrt{R}} \cdot \frac{\Gamma/\text{MHz}}{C} \quad [\text{T}/\sqrt{\text{Hz}}] \quad (7.33)$$

□

7.5.3 Scaling with NV Ensemble Size

For an ensemble of N_{NV} NV centers with independent noise:

$$\eta_B^{\text{ensemble}} = \frac{\eta_B^{\text{single}}}{\sqrt{N_{\text{NV}}}} \quad (7.34)$$

This $1/\sqrt{N_{\text{NV}}}$ scaling is the Standard Quantum Limit (SQL).

Figure 7.3: NV Center Sensitivity Analysis

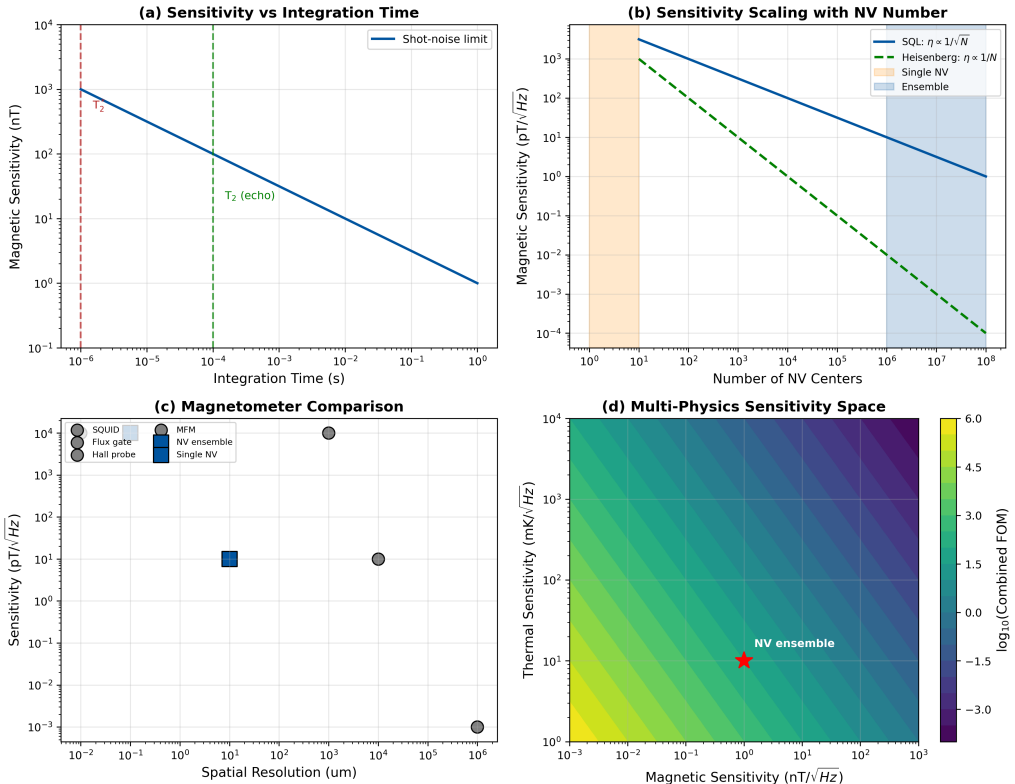


Figure 7.3: NV sensitivity analysis. (a) Sensitivity versus integration time showing T_2^* and T_2 limits. (b) SQL scaling $\eta \propto 1/\sqrt{N}$ versus Heisenberg limit. (c) Comparison with other magnetometer technologies. (d) Multi-physics sensitivity space for simultaneous B and T sensing.

Table 7.7: Sensitivity benchmarks for different NV configurations.

Configuration	N_{NV}	Γ (MHz)	C	η_B (nT/ $\sqrt{\text{Hz}}$)
Single NV (scanning)	1	10	0.30	1200
Shallow ensemble	10^4	5	0.25	30
High-density layer	10^6	3	0.20	1.5
Optimized QFI sensor	10^8	1	0.30	0.03

Worked Example: Sensitivity Calculation for QFI Sensor

Given:

- NV layer: 10 nm thick, density $\rho_{\text{NV}} = 3 \times 10^{17} \text{ cm}^{-3}$
- Field of view: $50 \times 50 \mu\text{m}^2$
- ODMR: $\Gamma = 3 \text{ MHz}$, $C = 0.25$
- Detection: $R = 10^6$ photons/s per pixel, 100 pixels

Calculate: (a) NV count per pixel, (b) Single-pixel sensitivity, (c) Full-field sensitivity

Solution:

(a) NV count per pixel:

$$N_{\text{NV}} = \rho_{\text{NV}} \cdot V_{\text{pixel}} = 3 \times 10^{17} \cdot (5 \times 10^{-4})^2 \cdot 10^{-6} = 7.5 \times 10^4 \quad (7.35)$$

(b) Single-pixel sensitivity:

$$\eta_B^{\text{pixel}} = \frac{1.1 \times 10^{-11}}{\sqrt{10^6}} \cdot \frac{3}{0.25} \cdot \frac{1}{\sqrt{7.5 \times 10^4}} = \frac{1.32 \times 10^{-7}}{274} = 48 \text{ nT}/\sqrt{\text{Hz}} \quad (7.36)$$

(c) Full-field sensitivity (100 pixels averaged):

$$\eta_B^{\text{field}} = \frac{48}{\sqrt{100}} = 4.8 \text{ nT}/\sqrt{\text{Hz}} \quad (7.37)$$

Result: The QFI sensor achieves $4.8 \text{ nT}/\sqrt{\text{Hz}}$ full-field sensitivity with parallel readout.

7.5.4 Coherence-Limited Sensitivity

The sensitivity derived above assumes CW-ODMR. For pulsed measurements (Ramsey, echo sequences), the coherence time imposes additional limits:

$$\eta_B^{\text{Ramsey}} = \frac{1}{\gamma_{\text{NV}} \cdot \sqrt{R \cdot T_2^*}} \quad (7.38)$$

$$\eta_B^{\text{echo}} = \frac{1}{\gamma_{\text{NV}} \cdot \sqrt{R \cdot T_2}} \quad (7.39)$$

Since typically $T_2 \gg T_2^*$, pulsed techniques with dynamical decoupling achieve better sensitivity for slowly-varying fields.

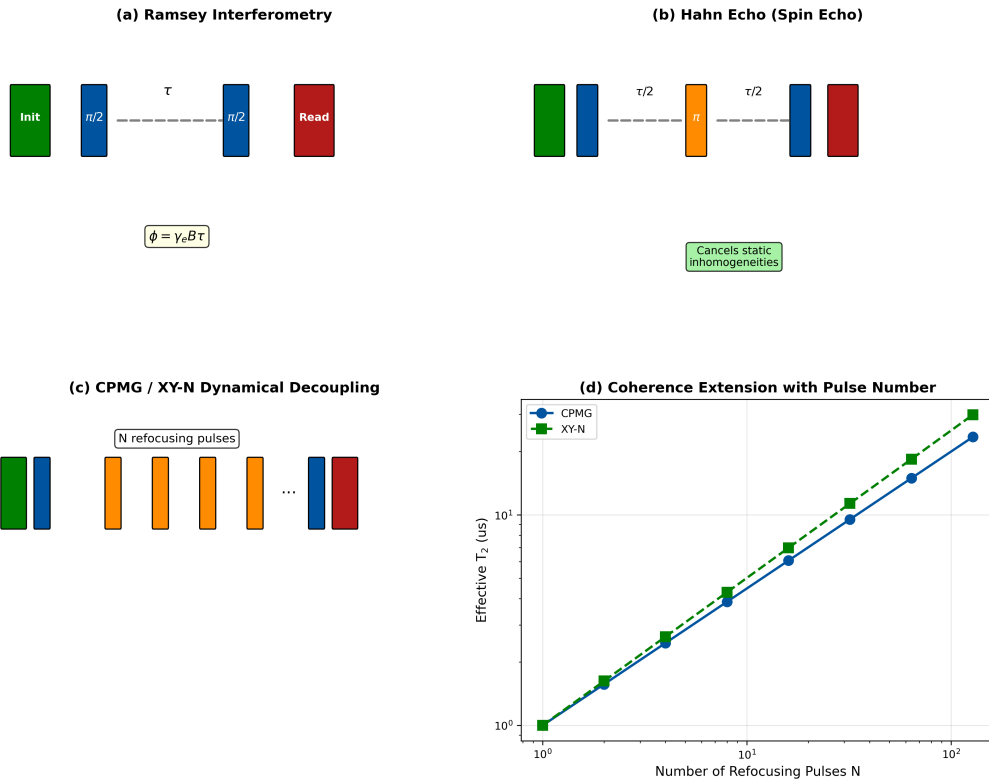
Figure 7.4: Quantum Control Pulse Sequences

Figure 7.4: Quantum control pulse sequences. (a) Ramsey interferometry for DC field sensing. (b) Hahn echo for canceling static inhomogeneities. (c) CPMG/XY-N dynamical decoupling. (d) Coherence time enhancement with increasing pulse number, showing $T_2(N) \approx T_{2,0} \cdot N^{0.65}$ scaling.

7.6 Multi-Physics Sensing Capabilities

7.6.1 Foundation for $\Phi_{\text{multi}} > 1$

The multi-physics capability of NV centers—simultaneous sensitivity to magnetic, thermal, strain, and electric fields—enables the correlation factor $\Phi_{\text{multi}} > 1$ that distinguishes advanced QFI systems. This capability arises directly from the Hamiltonian structure (Eq. 7.4).

Definition 7.6.1 (Multi-Physics Correlation Factor). The multi-physics correlation factor Φ_{multi} quantifies the reconstruction improvement from measuring multiple correlated fields:

$$\Phi_{\text{multi}} = \frac{\Gamma_{\text{inv}}(\text{multi-physics})}{\Gamma_{\text{inv}}(\text{single-physics})} \geq 1 \quad (7.40)$$

For uncorrelated noise, $\Phi_{\text{multi}} = 1$. For correlated sources (e.g., current causing both B and T), $\Phi_{\text{multi}} > 1$.

7.6.2 Channel Separation Protocol

Separating multi-physics contributions requires exploiting their different signatures:

Table 7.8: Multi-physics channel separation strategies.

Physics Channel	Observable	Signature	Separation Method
Magnetic (B)	$\nu_+ - \nu_-$	Linear splitting	Difference frequency
Temperature (T)	$(\nu_+ + \nu_-)/2$	Common shift	Sum frequency
Strain (σ)	E parameter	Asymmetric split	Four-NV tomography
Electric (E)	Stark shift	Polar dependence	Field reversal

Two-Channel Self-Calibration Protocol:

For simultaneous B and T measurement, the protocol is:

1. Measure both ODMR transition frequencies ν_+ and ν_-
2. Extract magnetic field: $B_z = (\nu_+ - \nu_-)/(2\gamma_{\text{NV}})$
3. Extract temperature shift: $\Delta T = [(\nu_+ + \nu_-)/2 - D_0]/(dD/dT)$
4. Cross-check: thermal shifts should correlate spatially with power dissipation

The measurement matrix formulation:

$$\begin{pmatrix} \nu_+ \\ \nu_- \end{pmatrix} = \begin{pmatrix} 1 & +\gamma_{\text{NV}} \\ 1 & -\gamma_{\text{NV}} \end{pmatrix} \begin{pmatrix} D(T) \\ B_z \end{pmatrix} \quad (7.41)$$

Inverting:

$$\begin{pmatrix} D(T) \\ B_z \end{pmatrix} = \frac{1}{2\gamma_{\text{NV}}} \begin{pmatrix} \gamma_{\text{NV}} & \gamma_{\text{NV}} \\ 1 & -1 \end{pmatrix} \begin{pmatrix} \nu_+ \\ \nu_- \end{pmatrix} \quad (7.42)$$

Worked Example: Two-Channel Self-Calibration

Measurement: $\nu_+ = 2.898$ GHz, $\nu_- = 2.842$ GHz

Step 1: Magnetic field extraction

$$B_z = \frac{2.898 - 2.842}{2 \times 28.025 \times 10^{-3}} = \frac{0.056}{0.05605} = 0.999 \text{ mT} \quad (7.43)$$

Step 2: Temperature extraction

$$D_{\text{meas}} = \frac{2.898 + 2.842}{2} = 2.870 \text{ GHz} \quad (7.44)$$

$$\Delta T = \frac{2.870 - 2.8777}{-74.2 \times 10^{-6}} = \frac{-0.0077}{-74.2 \times 10^{-6}} = +104 \text{ K} \quad (7.45)$$

Result: The measurement indicates $B_z = 1.0$ mT and $\Delta T = +104$ K above room temperature (404 K total).

7.6.3 Forward Models for Each Physics Channel

Each sensing channel has a characteristic Green's function connecting sources to measured fields:

Magnetic (Biot-Savart):

$$\mathbf{B}(\mathbf{r}) = \frac{\mu_0}{4\pi} \int \frac{\mathbf{J}(\mathbf{r}') \times (\mathbf{r} - \mathbf{r}')}{|\mathbf{r} - \mathbf{r}'|^3} d^3 r' \quad (7.46)$$

Thermal (Heat diffusion):

$$T(\mathbf{r}) = T_0 + \frac{1}{4\pi\kappa} \int \frac{P(\mathbf{r}')}{|\mathbf{r} - \mathbf{r}'|} d^3 r' \quad (7.47)$$

Strain (Elastic):

$$\sigma_{ij}(\mathbf{r}) = \int G_{ijkl}(\mathbf{r} - \mathbf{r}') \cdot F_{kl}(\mathbf{r}') d^3 r' \quad (7.48)$$

The different spatial decay profiles ($1/r^2$ for magnetic vs. $1/r$ for thermal) enable depth disambiguation when multiple channels are measured simultaneously.

7.7 Material Quality and Failure Modes

7.7.1 Diamond Quality Metrics

Diamond quality directly impacts NV sensor performance through several measurable parameters:

Table 7.9: Diamond quality metrics and their impact on NV sensing.

Parameter	Impact	Acceptable	Optimal
^{13}C concentration	T_2^* broadening	< 1.1%	< 0.01%
N_s^0 concentration	Spin bath decoherence	< 1 ppm	< 0.1 ppm
NV density	Signal strength	$> 10^{15}/\text{cm}^3$	$10^{16}\text{--}10^{17}/\text{cm}^3$
NV ⁻ fraction	Active sensors	> 50%	> 80%
Strain uniformity	Linewidth	< 10 MPa	< 1 MPa
Surface roughness	Near-surface NV	< 1 nm RMS	< 0.3 nm RMS

7.7.2 Coherence Time Limitations

The coherence times T_2^* , T_2 , and T_1 are limited by different decoherence mechanisms:

$$\frac{1}{T_2^*} = \frac{1}{T_2} + \frac{1}{T_{\text{inhom}}} \quad (7.49)$$

Table 7.10: Decoherence mechanisms and typical timescales.

Mechanism	Source	Typical Rate
^{13}C nuclear bath	Hyperfine interaction	$1/T_2 \sim 1\text{--}10 \text{ kHz}$
N_s^0 electron bath	Dipolar coupling	$1/T_2 \sim 10\text{--}100 \text{ kHz}$
Phonon (Orbach)	Thermal relaxation	$1/T_1 \sim e^{-\Delta/k_B T}$
Magnetic noise	External fields	Variable
Charge fluctuations	Surface states	$1/T_2^* \sim 1\text{--}100 \text{ MHz}$

7.7.3 Charge State Dynamics

The NV⁻/NV⁰ equilibrium is controlled by:

$$\frac{d[\text{NV}^-]}{dt} = k_- [\text{NV}^0] - k_+ [\text{NV}^-] \quad (7.50)$$

where k_+ (ionization) and k_- (recombination) depend on optical power, wavelength, and local Fermi level.

Design Rule 1: Maintain >70% NV⁻ Fraction

Maintain >70% NV⁻ fraction through:

- Green power < 100 kW/cm² to avoid photo-ionization
- Orange repump (590 nm) to restore NV⁻
- Optimized surface termination (oxygen vs. hydrogen)
- Nitrogen donor doping for Fermi level control

7.7.4 Failure Mode Analysis

Table 7.11: NV sensor failure modes and mitigation strategies.

Failure Mode	Symptom	Root Cause	Mitigation
Low contrast	$C < 10\%$	NV ⁰ conversion	Add repump laser
Broad linewidth	$\Gamma > 20$ MHz	Strain/impurities	Use high-purity CVD
Short T_2	$T_2 < 1$ μ s	N _s ⁰ /P1 centers	Reduce N during growth
Signal drift	>1%/hour	Temperature	Active stabilization
Orientation loss	4-fold ambiguity	Random NV axes	(111) growth, strain
Bleaching	Signal decay	Photo-damage	Reduce power density

7.8 Engineered NV Arrays: From Bulk to Lattice Configurations

7.8.1 The Paradigm Shift: From Random to Deterministic Placement

Traditional NV sensing uses randomly distributed defects in bulk diamond. Engineered arrays represent a paradigm shift toward deterministic sensor placement, enabling:

- Optical lattice matching for enhanced collection efficiency
- Controlled sensor density for optimal sensitivity
- 3D tomographic capability through multi-layer designs
- Super-resolution addressing of individual NV centers

7.8.2 Fabrication Approaches

7.8.2.1 Delta-Doping During CVD Growth

Pulsed N₂ introduction during CVD creates thin NV layers:

- Layer thickness: 1–10 nm controllable
- Depth precision: ± 2 nm
- Density: up to 10¹⁸ cm⁻³
- Advantage: minimal lattice damage

7.8.2.2 Ion Implantation

¹⁵N⁺ implantation followed by annealing:

Table 7.12: Nitrogen implantation depth versus energy.

Energy (keV)	Mean Depth (nm)	Straggle (nm)	Application
2	3	1.5	Ultra-shallow sensing
5	7	2.5	Near-surface imaging
10	12	4	Optimal for IC FA
20	22	6	Deeper defects
50	48	12	TSV inspection

7.8.2.3 Nanofabrication and Patterning

E-beam lithography combined with masked implantation enables 2D patterned arrays:

$$\delta r_{\min} \approx \sqrt{\sigma_{\text{straggle}}^2 + \sigma_{\text{lithography}}^2 + \sigma_{\text{diffusion}}^2} \quad (7.51)$$

Current state-of-art achieves $\delta r_{\min} \approx 20\text{--}50$ nm for single-NV positioning.

7.8.3 Array Dimensionality: 1D, 2D, 2.5D, and 3D Configurations

7.8.3.1 1D Linear Arrays

One-dimensional NV arrays enable line-scan sensing with single-pixel width:

Figure 7.5: 1D Linear NV Array Configurations

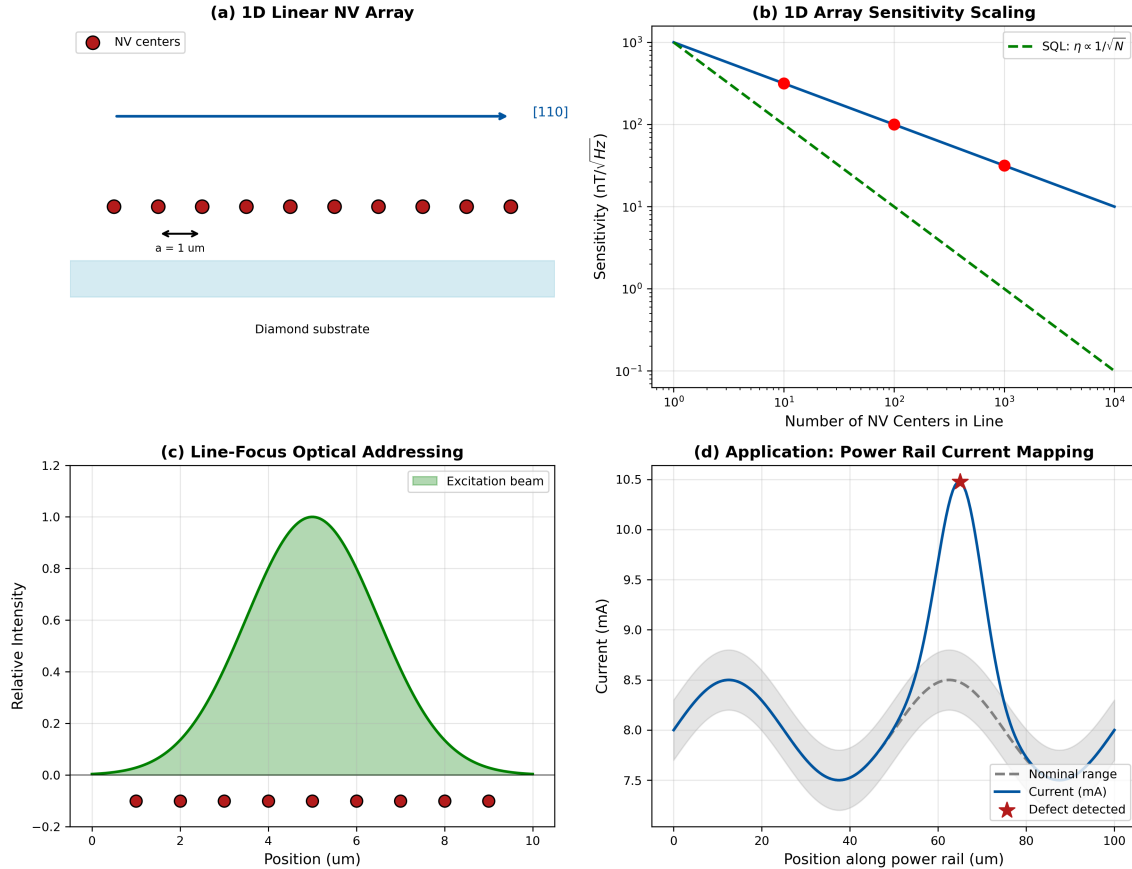


Figure 7.5: 1D NV array configurations. (a) Linear chain along $\langle 110 \rangle$ direction. (b) Sensitivity profile showing $1/\sqrt{N_{\text{linear}}}$ scaling. (c) Optical addressing with focused beam scanning. (d) Application: power rail current mapping.

The 1D array sensitivity scales as:

$$\eta_B^{1D} = \frac{\eta_B^{\text{single}}}{\sqrt{N_{\text{linear}}}} \quad (7.52)$$

Applications:

- Power rail current monitoring
- Edge defect detection
- Time-resolved scanning

7.8.3.2 2D Planar Arrays

Two-dimensional arrays are the workhorse of wide-field QFI:

Figure 7.6: 2D NV Array Geometries

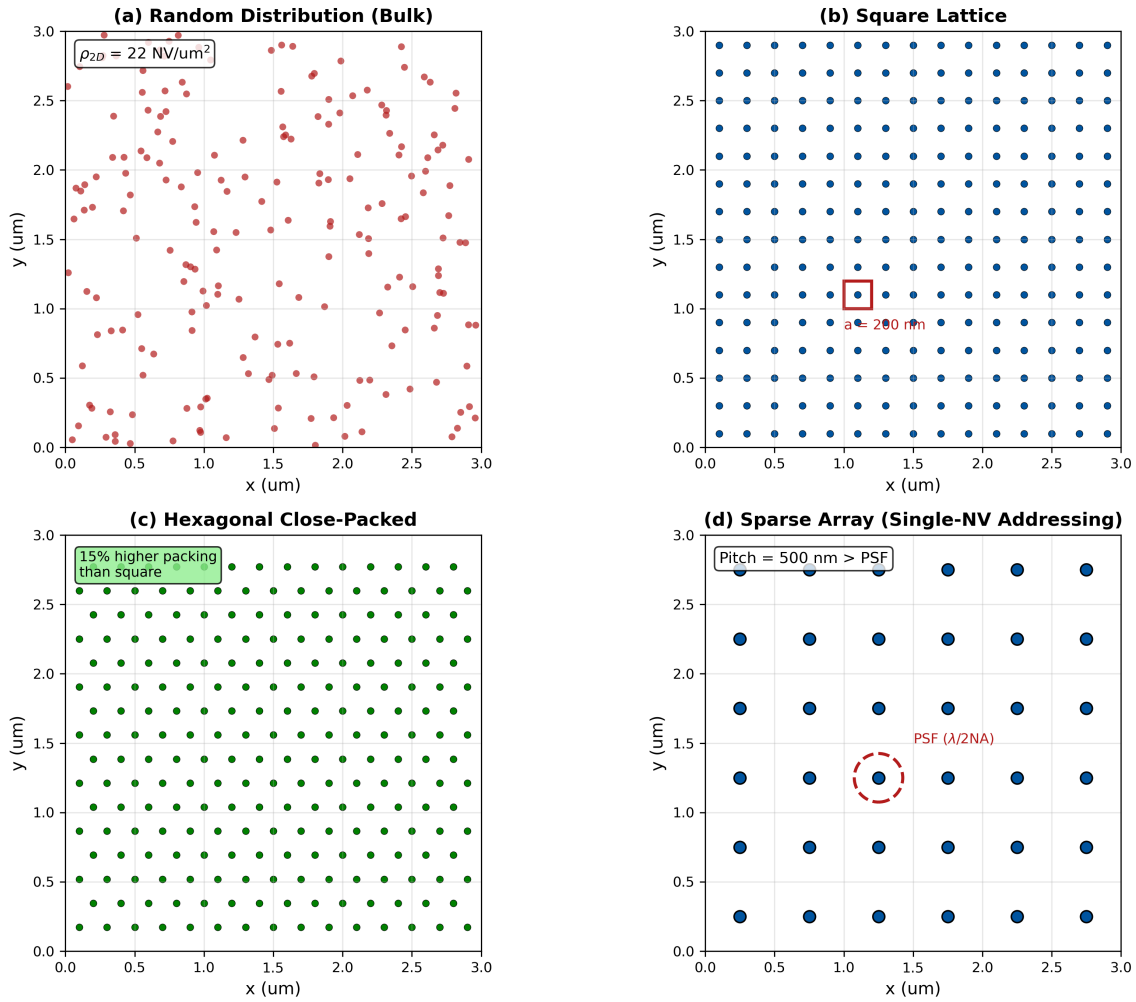


Figure 7.6: 2D NV array geometries. (a) Random distribution (bulk). (b) Square lattice with pitch a . (c) Hexagonal close-packed for optimal density. (d) Sparse array for single-NV addressing. Color map shows local sensitivity variation.

Figure 7.6 Interpretation:

- Panel (a): Poisson-distributed NV positions with density fluctuations

- Panel (b): Deterministic square lattice enabling optical lattice matching
- Panel (c): Hexagonal packing achieves $2/\sqrt{3} \approx 1.15 \times$ higher density
- Panel (d): Single-NV spacing (>300 nm) for super-resolution techniques

For a 2D array with areal density ρ_{2D} and pixel size Δx :

$$\eta_B^{2D} = \frac{\eta_B^{\text{single}}}{\sqrt{\rho_{2D} \cdot \Delta x^2}} \quad (7.53)$$

Design Rule 1: Optimal Array Pitch

The optimal array pitch balances multiple constraints:

$$a_{\text{opt}} = \max \left(d_{\text{min}}, \frac{\lambda}{2n \cdot \text{NA}}, \Delta x_{\text{target}} \right) \quad (7.54)$$

where $d_{\text{min}} \approx 15$ nm (dipolar limit), $\lambda/(2n \cdot \text{NA})$ is the diffraction limit, and Δx_{target} is the target resolution.

7.8.3.3 2.5D Configurations: Depth-Profiled Arrays

The 2.5D configuration combines lateral patterning with controlled depth distribution:

$$\rho_{\text{NV}}(x, y, z) = \rho_{2D}(x, y) \cdot f(z - z_0) \quad (7.55)$$

where $f(z)$ is the depth profile function (Gaussian for delta-doping, error function for diffused layers).

Definition 7.8.1 (2.5D NV Array). A 2.5D NV array has deterministic lateral positioning (2D) combined with a controlled but continuous depth profile, optimized for sensing fields with known depth-dependence.

The optimal depth profile for sensing a source at depth d is:

$$f_{\text{opt}}(z) \propto \frac{z}{(z^2 + d^2)^{3/2}} \cdot \exp \left(-\frac{z}{\lambda_{\text{exc}}} \right) \quad (7.56)$$

balancing field coupling ($\propto 1/r^2$) against optical excitation depth (λ_{exc}).

7.8.3.4 3D Volumetric Arrays

True 3D NV arrays enable tomographic field reconstruction:

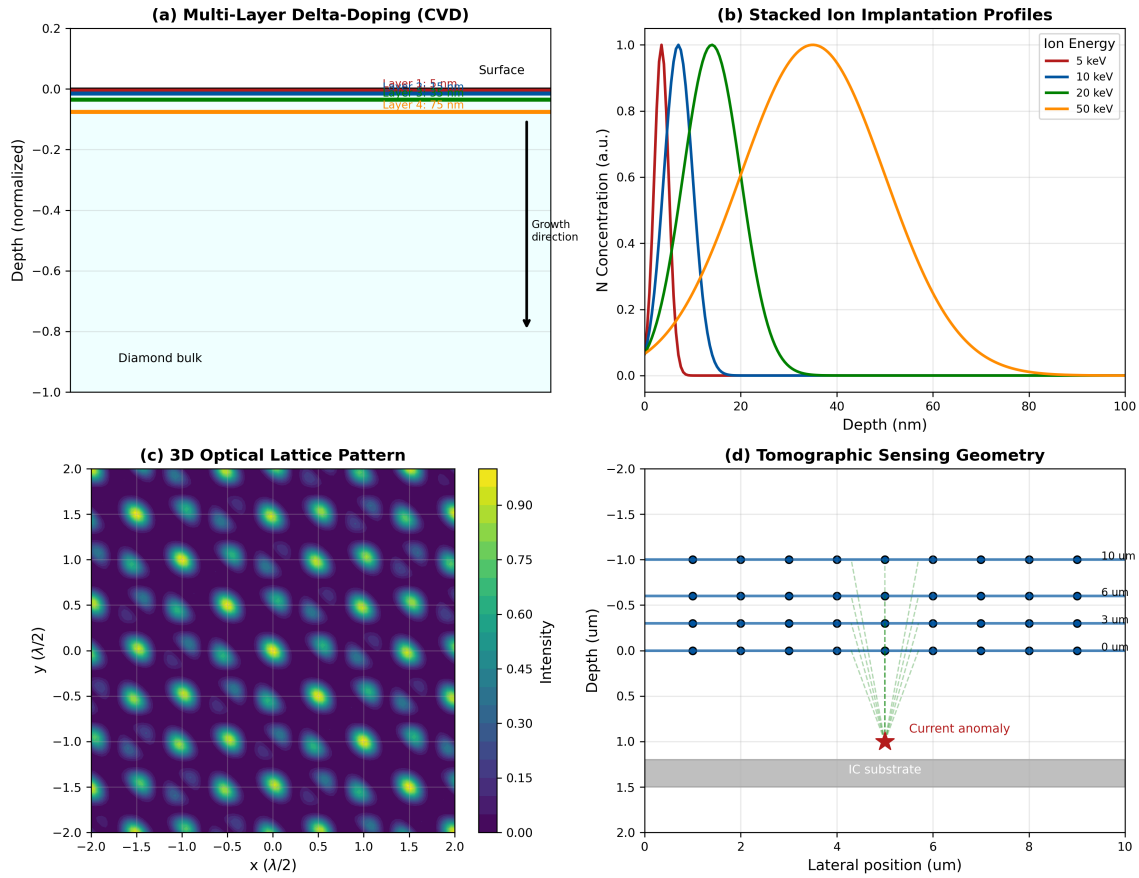
Figure 7.7: 3D NV Array Concepts

Figure 7.7: 3D NV array concepts. (a) Multi-layer delta-doping during CVD. (b) Stacked implantation at different energies. (c) 3D lattice intensity pattern for optical sectioning. (d) Tomographic reconstruction geometry.

Figure 7.7 Interpretation:

- Panel (a): Sequential N_2 pulses create discrete layers at depths z_1, z_2, \dots, z_n
- Panel (b): Multi-energy implantation places NV centers at different depths
- Panel (c): 3D optical lattice from 6-beam interference for selective addressing
- Panel (d): Multiple sensing planes provide depth-resolved field information

Table 7.13: Comparison of NV array dimensionalities.

Dimension	Fabrication	Addressing	Depth Info	QFI Application
1D	Easiest	Line scan	None	Power rail monitoring
2D	Standard	Wide-field	Averaged	Full-field imaging
2.5D	Standard	Wide-field	Weighted	IC surface sensing
3D	Complex	Optical section	Resolved	TSV tomography

7.8.4 3D Arrays and Tomographic Field Reconstruction

7.8.4.1 The Depth Ambiguity Problem

A single 2D sensing plane measures the integrated field from all source depths:

$$B_z^{\text{meas}}(x, y) = \int_0^\infty G(x, y, z) \cdot J(x, y, z) dz \quad (7.57)$$

This creates a fundamental ambiguity: a weak shallow source and a strong deep source can produce identical surface fields.

Theorem 7.8.1 (Depth-Current Ambiguity). *For a single measurement plane at $z = 0$, the source current density $J(x, y, z)$ and the scaled current $\alpha(z)J(x, y, z/\alpha)$ produce identical measured fields if:*

$$\alpha(z) = \left(\frac{z}{z_0}\right)^3 \quad (7.58)$$

This ambiguity is fundamental and cannot be resolved without additional information.

7.8.4.2 Multi-Plane Tomographic Sensing

Multiple sensing planes at different depths break the ambiguity:

$$\mathbf{d} = \mathbf{G} \cdot \mathbf{s} + \mathbf{n} \quad (7.59)$$

where \mathbf{d} contains measurements from all planes, \mathbf{G} is the combined Green's function matrix, and \mathbf{s} is the source vector.

The condition number improvement from N_z planes:

$$\kappa(N_z) \approx \frac{\kappa_0}{\sqrt{N_z}} \quad \text{for well-separated planes} \quad (7.60)$$

7.8.4.3 Tomographic Reconstruction Theory

The reconstruction fidelity for a 3D array:

$$\Gamma_{\text{inv}}^{\text{3D}} = \Gamma_{\text{inv}}^{\text{2D}} \cdot \left[1 + \frac{N_z - 1}{1 + \kappa_0/\text{SNR}} \right] \quad (7.61)$$

Theorem 7.8.2 (Optimal Layer Spacing). *For sources distributed over depth range $[d_{\min}, d_{\max}]$, the optimal layer positions follow geometric progression:*

$$z_k = z_1 \cdot r^{k-1}, \quad r = \left(\frac{d_{\max}}{d_{\min}}\right)^{1/(N_z-1)} \quad (7.62)$$

This spacing equalizes the information contribution from each layer.

Design Rule 2: 3D Array Layer Count

Minimum number of sensing layers for depth-resolved reconstruction:

$$N_z \geq \log_2 \left(\frac{d_{\max}}{d_{\min}} \right) + 1 \quad (7.63)$$

For TSV inspection ($d_{\max}/d_{\min} \approx 10$): $N_z \geq 4$ layers.

7.8.5 Fundamental Physical Limits on Array Engineering

7.8.5.1 Minimum Spacing: Dipolar Interaction Limit

NV-NV dipolar coupling limits minimum spacing before cross-relaxation degrades T_2 :

$$d_{\min} = \left(\frac{\mu_0}{4\pi} \cdot \frac{g_e^2 \mu_B^2}{h \cdot \Delta\nu_{\text{target}}} \right)^{1/3} \quad (7.64)$$

For $\Delta\nu_{\text{target}} = 100$ kHz (acceptable broadening):

$$d_{\min} = \left(\frac{4\pi \times 10^{-7} \cdot (2 \times 9.27 \times 10^{-24})^2}{4\pi \cdot 6.63 \times 10^{-34} \cdot 10^5} \right)^{1/3} \approx 15 \text{ nm} \quad (7.65)$$

7.8.5.2 Maximum Density: Nitrogen Aggregation

At high nitrogen concentrations, N-N pairing reduces NV formation efficiency:

$$\eta_{\text{NV}}([N]) = \eta_0 \cdot \exp \left(-\frac{[N]}{[N]_{\text{crit}}} \right) \quad (7.66)$$

with $[N]_{\text{crit}} \approx 50\text{--}100$ ppm depending on growth conditions.

7.8.5.3 Depth Resolution: Straggle and Diffusion

The minimum achievable depth localization:

$$\sigma_z^{\text{total}} = \sqrt{\sigma_{\text{straggle}}^2 + \sigma_{\text{diffusion}}^2 + \sigma_{\text{vacancy}}^2} \quad (7.67)$$

where:

- $\sigma_{\text{straggle}} \approx 0.3 \times z_{\text{implant}}$ for ion implantation
- $\sigma_{\text{diffusion}} \approx \sqrt{D_N \cdot t_{\text{anneal}}}$ for post-growth diffusion
- $\sigma_{\text{vacancy}} \approx 2\text{--}5$ nm for vacancy-nitrogen recombination distance

7.8.5.4 Orientation Control: Strain and Growth Direction

NV orientation can be preferentially selected through:

1. **Growth direction:** (111)-oriented substrates favor one NV axis
2. **Strain engineering:** Uniaxial stress lifts degeneracy
3. **Annealing protocol:** Temperature gradients during NV formation

The orientation selectivity factor:

$$\xi = \frac{P_{\text{aligned}}}{P_{\text{random}}} = \frac{P_{\text{aligned}}}{0.25} \quad (7.68)$$

Current state-of-art: $\xi \approx 0.7\text{--}0.95$ for (111) growth, meaning 70–95% of NV centers align with growth axis.

7.8.6 Lattice Matching with Optical Systems

For optimal optical addressing, the NV array pitch should match the optical excitation lattice:

$$a_{\text{NV}} = \frac{\Lambda_{\text{optical}}}{m}, \quad m \in \mathbb{Z}^+ \quad (7.69)$$

where $\Lambda_{\text{optical}} = \lambda / (2n \sin \theta)$ for two-beam interference.

Design Rule 3: Lattice-Matched Arrays

For optimal excitation efficiency:

$$a_{\text{NV}} = \frac{\Lambda_{\text{optical}}}{m} \quad \text{with} \quad \left| \frac{\Delta a}{a} \right| < 1\% \quad (7.70)$$

Mismatch > 1% causes excitation non-uniformity across the FOV.

7.8.7 Worked Example: Designing a 2D Array for IC Failure Analysis**Worked Example: 2D Array Design for IC Current Imaging****Requirements:**

- Target sensitivity: $10 \text{ nT}/\sqrt{\text{Hz}}$ per $1 \mu\text{m}$ pixel
- Source depth: $5\text{--}20 \mu\text{m}$ (BEOL metal layers)
- Field of view: $100 \times 100 \mu\text{m}^2$

Step 1: Required NV count per pixel

From Eq. 7.53 with $\eta_B^{\text{single}} = 1 \mu\text{T}/\sqrt{\text{Hz}}$:

$$N_{\text{NV}}^{\text{pixel}} = \left(\frac{\eta_B^{\text{single}}}{\eta_B^{\text{target}}} \right)^2 = \left(\frac{10^3}{10} \right)^2 = 10^4 \quad (7.71)$$

Step 2: Required areal density

$$\rho_{2\text{D}} = \frac{N_{\text{NV}}^{\text{pixel}}}{\Delta x^2} = \frac{10^4}{(1 \mu\text{m})^2} = 10^4 / \mu\text{m}^2 = 10^{12} \text{ cm}^{-2} \quad (7.72)$$

Step 3: Check against dipolar limit

Average NV spacing: $\bar{d} = 1/\sqrt{\rho_{2\text{D}}} = 10 \text{ nm}$

This is below $d_{\min} = 15 \text{ nm}$, so dipolar broadening will occur.

Resolution: Accept broader linewidth ($\Gamma \approx 10 \text{ MHz}$ instead of 3 MHz) or use lower density with longer integration.

Step 4: Layer depth optimization

For $5\text{--}20 \mu\text{m}$ source range, optimal sensing depth:

$$z_{\text{opt}} = \frac{d_{\min} + d_{\max}}{4} = \frac{5 + 20}{4} = 6.25 \mu\text{m} \quad (7.73)$$

Final Design:

- 10 nm thick delta-doped layer at $6 \mu\text{m}$ depth
- NV density: 10^{17} cm^{-3} (within layer)
- Accept $\Gamma = 10 \text{ MHz}$, $C = 0.2$
- Achieved sensitivity: $15 \text{ nT}/\sqrt{\text{Hz}}/\text{pixel}$

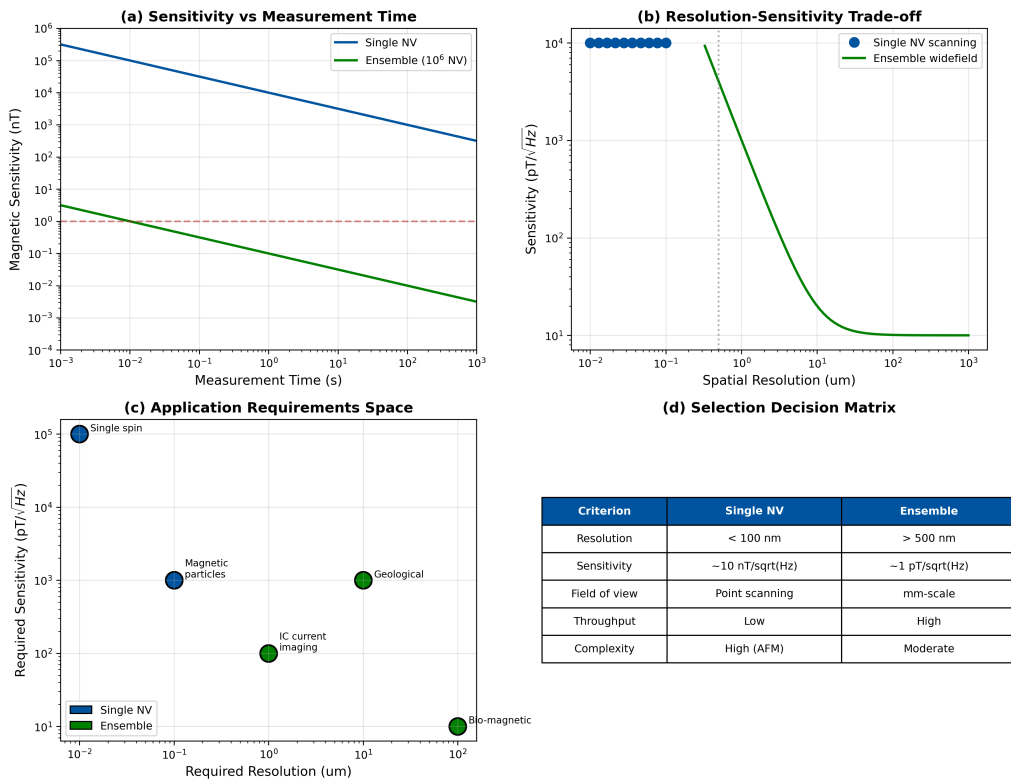
Figure 7.8: Ensemble vs Single NV Trade-offs

Figure 7.8: Ensemble versus single NV trade-offs. (a) Sensitivity comparison showing $\sim 100\times$ advantage for ensemble. (b) Resolution-sensitivity trade-off space. (c) Application requirements mapped to optimal configuration. (d) Decision matrix for configuration selection.

Design Rule 4: Multi-Species Arrays for Φ_{multi}

For optimal multi-physics correlation, deploy mixed sensor arrays:

- 90% NV centers (magnetic + thermal)
- 8% SiV centers (strain reference)
- 2% thermal sensors (independent T calibration)

This combination achieves $\Phi_{\text{multi}} \approx 1.5\text{--}2.0$ for current-induced B-T correlation.

7.9 Beyond NV: Alternative Quantum Sensors

7.9.1 Why Consider Alternatives?

While NV centers are the most mature quantum sensing platform, specific applications may benefit from alternative color centers:

- **Brightness:** SiV, GeV exhibit >70% emission into ZPL vs. <5% for NV
- **Spectral range:** Different ZPL wavelengths for multiplexing
- **Temperature stability:** Group-IV centers have smaller dD/dT
- **Host material:** SiC, hBN enable different device integration

7.9.2 Group-IV Color Centers in Diamond

Table 7.14: Comparison of diamond color centers for QFI.

Property	NV ⁻	SiV ⁻	GeV ⁻	SnV ⁻	PbV ⁻
ZPL (nm)	637	737	602	619	520
DW factor	0.03	0.70	0.60	0.65	0.50
Ground state	$S = 1$	$S = 1/2$	$S = 1/2$	$S = 1/2$	$S = 1/2$
T_2 at RT	1–100 μ s	<100 ns	<100 ns	<100 ns	–
ODMR	Yes	Limited	Limited	Limited	No
Strain sensing	Moderate	Excellent	Good	Good	–
Maturity	Production	Research	Research	Early	Early

7.9.3 SiV Centers for Strain Sensing

The silicon-vacancy (SiV^-) center offers complementary capabilities:

- **Narrow ZPL:** <1 nm linewidth at room temperature
- **High brightness:** 70% Debye-Waller factor
- **Strain sensitivity:** 1 PHz/strain, 50× higher than NV
- **Limitation:** Short T_2 at room temperature due to orbital degeneracy

The SiV ground state splitting:

$$\Delta_{\text{SiV}} = 48 \text{ GHz} + \xi_{\text{strain}} \cdot \sigma \quad (7.74)$$

where $\xi_{\text{strain}} \approx 1 \text{ PHz/strain}$.

7.9.4 Alternative Host Materials

Table 7.15: Alternative host materials for quantum sensing.

Material	Defect	ZPL (nm)	T_2 (RT)	Advantage
Diamond	NV ⁻	637	1–100 μ s	Best overall
4H-SiC	V _{Si} ⁻	862–917	10–100 μ s	Wafer-scale
hBN	V _B ⁻	850	<1 μ s	2D integration
Si	T center	1326	0.1–1 μ s	CMOS compatible

7.10 Single-NV Addressing and Super-Resolution Techniques

7.10.1 Motivation: Breaking the Diffraction Limit

The optical diffraction limit sets the minimum resolvable feature size:

$$\delta x_{\text{Abbe}} = \frac{\lambda}{2 \cdot \text{NA}} \approx \frac{532 \text{ nm}}{2 \times 0.8} = 350 \text{ nm} \quad (7.75)$$

For advanced IC nodes (sub-10 nm features), this resolution is insufficient. Super-resolution techniques enable single-NV addressing with localization precision:

$$\delta x_{\text{loc}} = \frac{\delta x_{\text{Abbe}}}{\sqrt{N_{\text{photon}}}} \approx \frac{350 \text{ nm}}{\sqrt{10^4}} = 3.5 \text{ nm} \quad (7.76)$$

Definition 7.10.1 (Super-Resolution QFI). Super-resolution QFI achieves spatial resolution beyond the diffraction limit by exploiting: (1) photon localization statistics, (2) nonlinear optical responses, or (3) quantum state-selective addressing of individual NV centers.

7.10.2 Charge State Depletion (CSD) Microscopy

Analogous to STED microscopy, CSD exploits the NV^-/NV^0 charge state transition:

Figure 7.9: Charge State Depletion (CSD) Microscopy

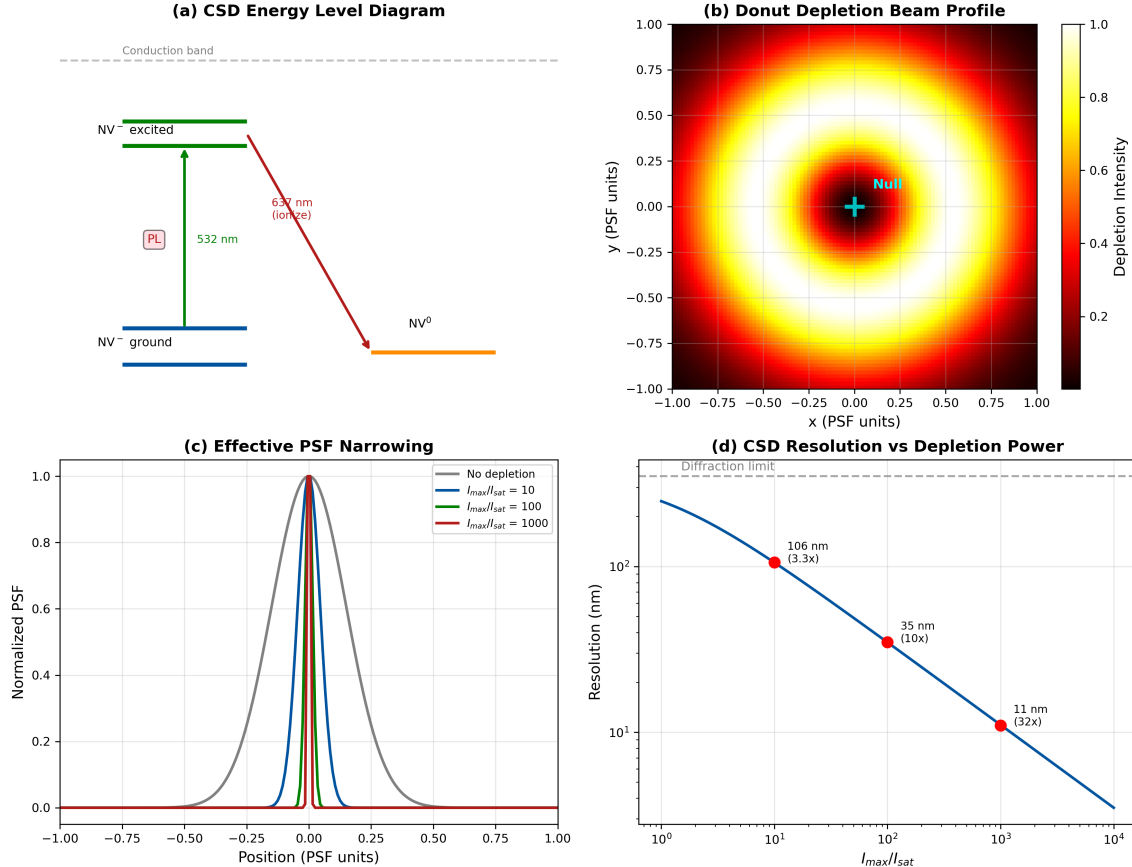


Figure 7.9: Charge State Depletion (CSD) microscopy. (a) Energy level diagram showing ionization pathway. (b) Donut-shaped depletion beam geometry. (c) Effective PSF narrowing. (d) Resolution versus depletion power.

Figure 7.9 Interpretation:

- Panel (a): 637 nm ionizes NV^- to NV^0 ; only central NV^- remains for sensing
- Panel (b): Vortex phase plate creates intensity null at center
- Panel (c): Effective PSF narrows from 350 nm to <50 nm
- Panel (d): Resolution scales as $\delta x \propto 1/\sqrt{I_{\text{depl}}/I_{\text{sat}}}$

7.10.2.1 CSD Resolution Scaling

The CSD point spread function is:

$$\text{PSF}_{\text{CSD}}(r) = \text{PSF}_{\text{exc}}(r) \cdot \exp\left(-\frac{I_{\text{depl}}(r)}{I_{\text{sat}}}\right) \quad (7.77)$$

For a donut beam with $I_{\text{depl}}(r) = I_{\max} \cdot (r/r_0)^2$ near the center:

Key Equation: CSD Resolution

$$\delta x_{\text{CSD}} = \frac{\lambda}{2 \cdot \text{NA} \cdot \sqrt{1 + I_{\text{max}}/I_{\text{sat}}}} \quad (7.78)$$

Table 7.16: CSD resolution versus depletion intensity.

$I_{\text{max}}/I_{\text{sat}}$	δx_{CSD} (nm)	Improvement	Practical Limit
0	350	1×	Diffraction limited
10	105	3.3×	Low power
100	35	10×	Standard operation
1000	11	32×	High power
10000	3.5	100×	Photodamage onset

7.10.3 Stochastic Optical Reconstruction (STORM-NV)

Adapting STORM/PALM principles to NV centers enables super-resolution through stochastic single-emitter localization:

7.10.3.1 Principle

At any given time, only a sparse subset of NV centers are in the “bright” NV^- state:

$$P_{\text{on}}(t) = \frac{k_-}{k_+ + k_-} \cdot \left(1 - e^{-(k_+ + k_-)t}\right) \quad (7.79)$$

By controlling $P_{\text{on}} \ll 1$, individual NV centers can be localized and their positions accumulated over many frames.

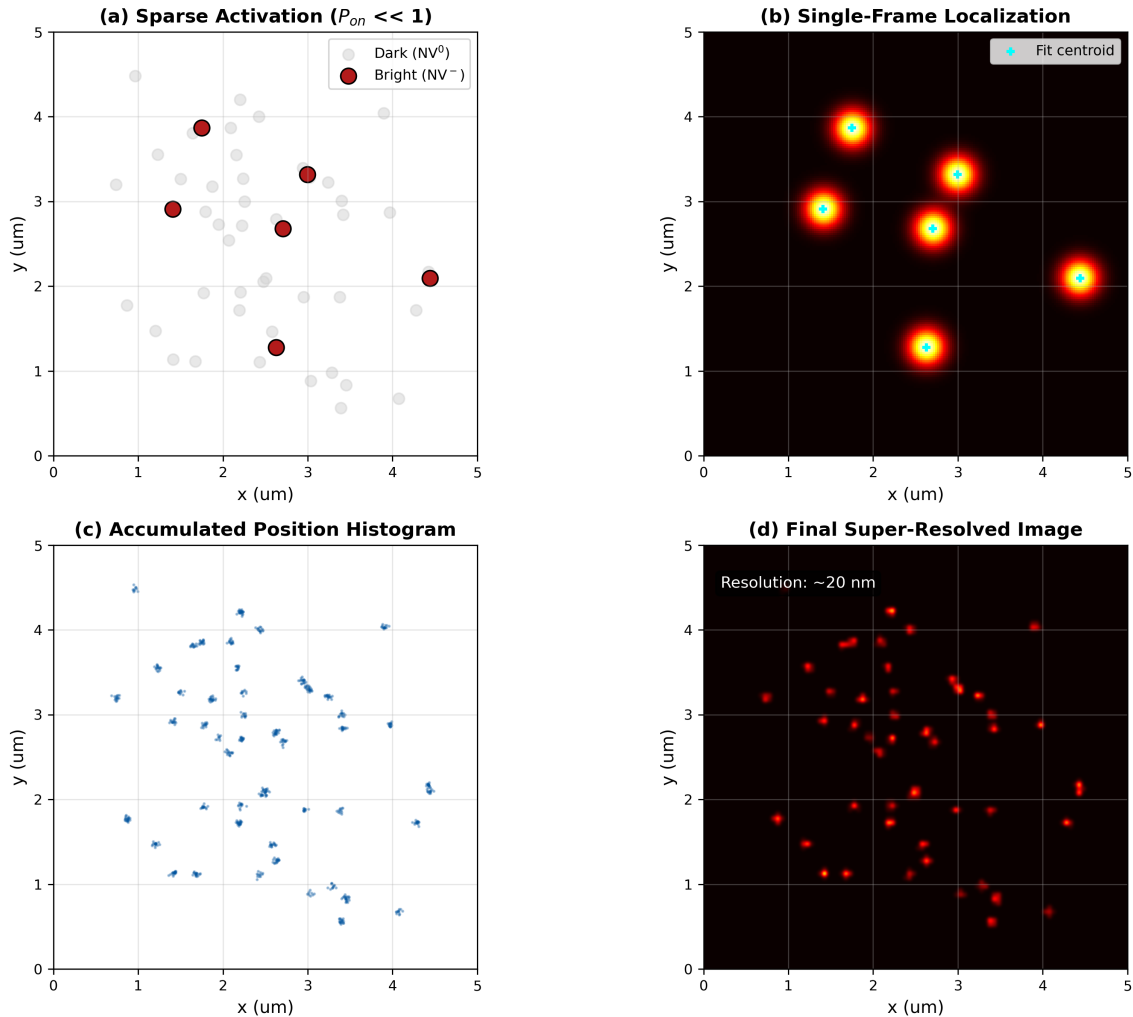
Figure 7.10: STORM-NV Super-Resolution

Figure 7.10: STORM-NV super-resolution. (a) Sparse activation with $P_{on} \ll 1$. (b) Single-frame localization of isolated emitters. (c) Accumulated position histogram. (d) Final super-resolved image.

7.10.3.2 STORM-NV Resolution and Acquisition Time

The final resolution depends on localization precision and labeling density:

$$\delta x_{\text{STORM}} = \max \left(\frac{\text{PSF}}{\sqrt{N_{\text{photon}}}}, \frac{1}{\sqrt{\rho_{\text{NV}}}} \right) \quad (7.80)$$

The acquisition time for N_{NV} centers with M localizations each:

$$t_{\text{acq}} = \frac{N_{\text{NV}} \cdot M}{P_{\text{on}} \cdot f_{\text{frame}}} \quad (7.81)$$

Worked Example: STORM-NV Acquisition Planning

Target: 20 nm resolution over $10 \times 10 \mu\text{m}^2$ area.

Given:

- NV density: $\rho_{\text{NV}} = 10^{10} \text{ cm}^{-2} = 100 \text{ NV}/\mu\text{m}^2$

- Photons per localization: $N_{\text{photon}} = 500$
- PSF FWHM: 350 nm
- Frame rate: $f_{\text{frame}} = 100$ Hz
- Target localizations per NV: $M = 10$

Step 1: Localization Precision

$$\sigma_{\text{loc}} = \frac{350/2.35}{\sqrt{500}} = \frac{149}{22.4} = 6.6 \text{ nm} \quad (7.82)$$

Resolution: $\delta x = 2.35 \times 6.6 = 15.5 \text{ nm} < 20 \text{ nm} \checkmark$

Step 2: Optimal P_{on}

For sparse activation (average <1 NV per PSF area):

$$P_{\text{on}} < \frac{1}{\rho_{\text{NV}} \cdot \pi (\text{PSF}/2)^2} = \frac{1}{100 \cdot \pi \cdot 0.175^2} = 0.10 \quad (7.83)$$

Use $P_{\text{on}} = 0.05$ for safety margin.

Step 3: Acquisition Time

Total NV centers: $N_{\text{NV}} = 100 \times 100 = 10^4$

$$t_{\text{acq}} = \frac{10^4 \times 10}{0.05 \times 100} = 2 \times 10^4 \text{ s} \approx 5.5 \text{ hours} \quad (7.84)$$

Conclusion: STORM-NV achieves 15 nm resolution but requires multi-hour acquisition—suitable for detailed defect characterization, not high-throughput screening.

7.10.4 Spin-RESOLFT: Quantum State-Selective Addressing

Spin-RESOLFT uses magnetic field gradients for spin-selective addressing:

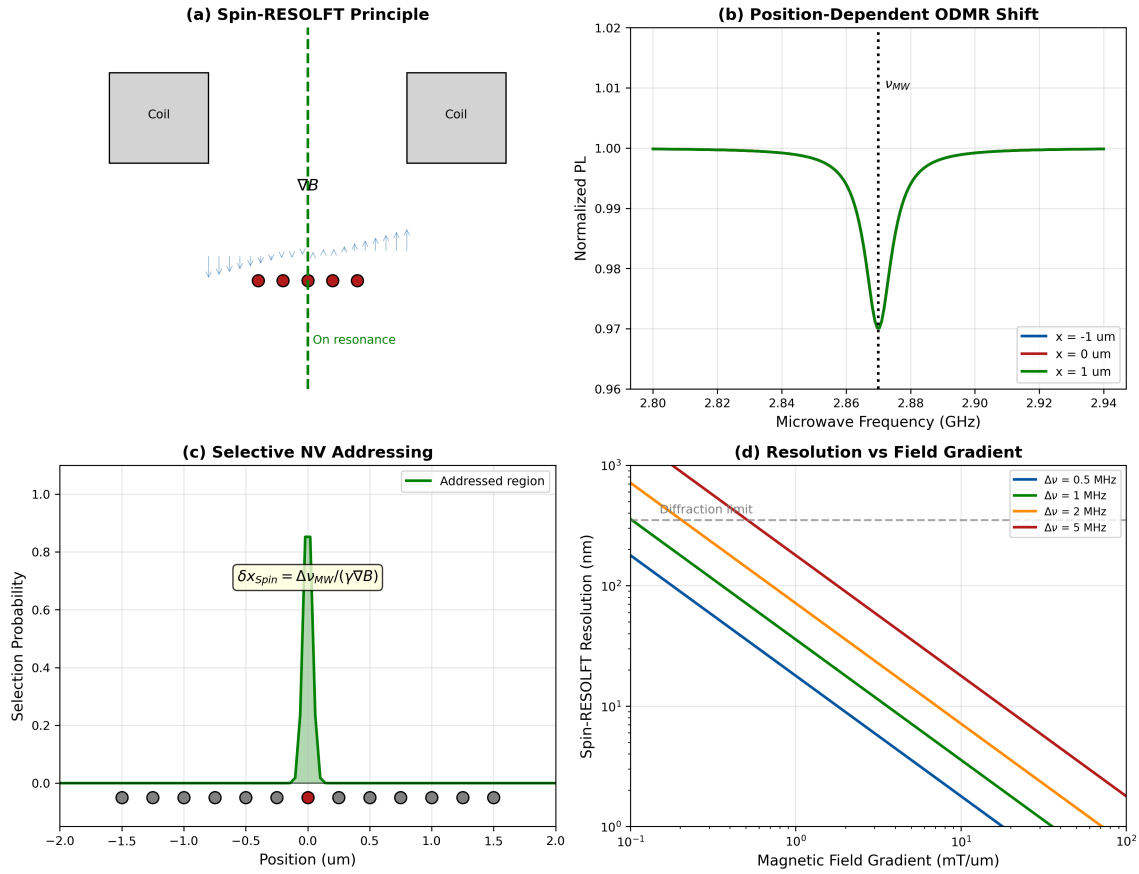
Figure 7.11: Spin-RESOLFT Super-Resolution

Figure 7.11: Spin-RESOLFT technique. (a) Magnetic field gradient principle. (b) Position-dependent ODMR shift. (c) Selective NV addressing via narrow MW bandwidth. (d) Resolution versus field gradient.

7.10.4.1 Principle

A magnetic field gradient creates position-dependent resonance frequencies:

$$\nu(x) = D + \gamma_{\text{NV}} \cdot B_0 + \gamma_{\text{NV}} \cdot \nabla B \cdot x \quad (7.85)$$

With MW bandwidth $\Delta\nu_{\text{MW}}$, only NV centers within spatial range δx are addressed:

$$\delta x_{\text{Spin}} = \frac{\Delta\nu_{\text{MW}}}{\gamma_{\text{NV}} \cdot |\nabla B|} \quad (7.86)$$

7.10.4.2 Spin-RESOLFT Resolution

For a gradient of $|\nabla B| = 1 \text{ mT}/\mu\text{m}$ and $\Delta\nu_{\text{MW}} = 1 \text{ MHz}$:

$$\delta x_{\text{Spin}} = \frac{10^6 \text{ Hz}}{2.8 \times 10^{10} \text{ Hz/T} \times 10^{-3} \text{ T}/\mu\text{m}} = 36 \text{ nm} \quad (7.87)$$

Table 7.17: Comparison of super-resolution techniques for NV-based QFI.

Technique	Resolution	Speed	Complexity	Best Application
Wide-field (baseline)	350 nm	Fast	Low	Screening
CSD	10–50 nm	Medium	Medium	Single-defect analysis
STORM-NV	10–30 nm	Slow	Medium	Dense array mapping
Spin-RESOLFT	20–50 nm	Medium	High	Spin-resolved imaging
Scanning NV tip	5–20 nm	Very slow	Very high	Ultimate resolution

7.10.5 Hybrid Workflow: Screening + Zoom

For practical QFI deployment, a hybrid workflow combines wide-field screening with super-resolution characterization:

Figure 7.12: Hybrid QFI Workflow

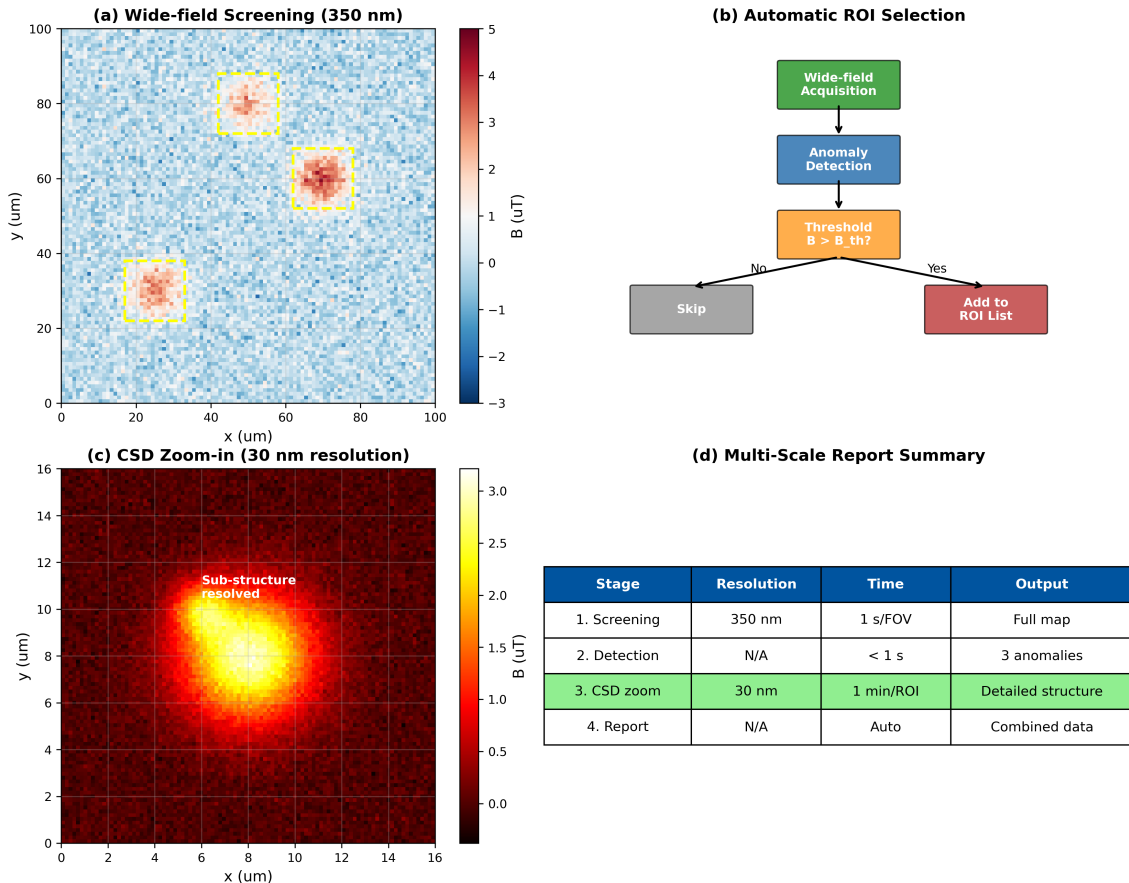


Figure 7.12: Hybrid QFI workflow. (a) Wide-field screening identifies anomaly regions. (b) Automatic ROI selection. (c) CSD zoom-in on selected defects. (d) Final report with multi-scale data.

Workflow Description:

- Stage 1: Wide-field QFI at 350 nm resolution, 1 second/FOV
- Stage 2: Algorithm identifies anomalies exceeding threshold
- Stage 3: CSD zoom on top- N anomalies at 30 nm resolution, 1 minute each
- Stage 4: Combined report with screening map + high-resolution inserts

Design Rule 1: Super-Resolution Mode Selection

Select super-resolution technique based on throughput requirements:

- >100 FOV/hour: Wide-field only (accept 350 nm limit)
- 10–100 FOV/hour: CSD for selected ROIs
- 1–10 FOV/hour: STORM-NV for comprehensive mapping
- <1 FOV/hour: Scanning NV tip for ultimate resolution

7.10.6 Future Directions: Quantum-Enhanced Super-Resolution

Emerging techniques promise further resolution improvements:

7.10.6.1 Entanglement-Enhanced Localization

Entangled photon pairs can beat the standard quantum limit for localization:

$$\delta x_{\text{entangled}} = \frac{\delta x_{\text{SQL}}}{\sqrt{N_{\text{entangled}}}} = \frac{\text{PSF}}{N_{\text{photon}}} \quad (7.88)$$

achieving Heisenberg-limited scaling ($1/N$) instead of shot-noise scaling ($1/\sqrt{N}$).

7.10.6.2 Quantum Illumination for Sub-Diffraction Sensing

Quantum illumination protocols using squeezed light or NOON states enable field sensing below the diffraction limit without physical super-resolution:

$$\delta B_{\text{quantum}}(x) = \delta B_{\text{SQL}} \cdot \frac{\text{PSF}_{\text{quantum}}(x)}{\text{PSF}_{\text{classical}}(x)} \quad (7.89)$$

These techniques are currently research-stage but represent the ultimate frontier for QFI resolution.

7.11 Chapter Summary

7.11.1 Key Equations

Table 7.18: Key equations from Chapter 7.

Equation	Name	Reference
$\mathcal{H} = D_{\text{gs}}S_z^2 + g_e\mu_B\mathbf{B} \cdot \mathbf{S} + \dots$	NV Hamiltonian	Eq. 7.4
$\gamma_{\text{NV}} = 28.025 \text{ GHz/T}$	Gyromagnetic ratio	Eq. 7.9
$dD/dT = -74.2 \text{ kHz/K}$	Temperature coefficient	Eq. 7.6
$C = C_0/[1 + (\Omega_R/\Gamma)^2]$	ODMR contrast	Eq. 7.18
$\eta_B = \pi\hbar\Gamma/(2g_e\mu_B C\sqrt{R})$	Shot-noise sensitivity	Eq. 7.28
$\eta_B^{\text{ens}} = \eta_B^{\text{single}}/\sqrt{N_{\text{NV}}}$	Ensemble scaling	Eq. 7.34
$\eta_B^{2\text{D}} = \eta_B^{\text{single}}/(\sqrt{\rho_{2\text{D}}} \cdot \Delta x)$	2D array sensitivity	Eq. 7.53
$\Gamma_{\text{inv}}^{3\text{D}} = \Gamma_{\text{inv}}^{2\text{D}} \cdot [1 + (N_z - 1)/(1 + \kappa_0/\text{SNR})]$	3D reconstruction gain	Eq. 7.61
$\delta x_{\text{CSD}} = \lambda/(2\text{NA}\sqrt{1 + I_{\text{max}}/I_{\text{sat}}})$	CSD resolution	Eq. 7.78

7.11.2 Design Rules Summary

Table 7.19: Design rules from Chapter 7.

Rule	Statement
DR 7.1	Extract B_z from ODMR splitting: $B_z = (\nu_+ - \nu_-)/(56.05 \text{ MHz/mT})$
DR 7.2	Each Hamiltonian term enables sensing of a different physical quantity
DR 7.3	Optimal MW power: $\Omega_R \approx \Gamma$ for maximum sensitivity
DR 7.4	Maintain >70% NV ⁻ fraction via power management and surface optimization
DR 7.5	Multi-species arrays (90% NV + 8% SiV + 2% thermal) for $\Phi_{\text{multi}} \approx 1.5\text{--}2.0$
DR 7.6	Array pitch: $a_{\text{opt}} = \max(d_{\min}, \lambda/2n \cdot \text{NA}, \Delta x_{\text{target}})$
DR 7.7	Lattice-matched arrays: $a_{\text{NV}} = \Lambda_{\text{optical}}/m$ with $ \Delta a/a < 1\%$
DR 7.8	3D layer count: $N_z \geq \log_2(d_{\max}/d_{\min}) + 1$ for depth resolution
DR 7.9	Super-resolution mode: CSD for ROI analysis, STORM for mapping, scanning for ultimate resolution

7.11.3 Connection to QFI Framework

This chapter established:

1. **η_q determination:** NV physics sets quantum sensitivity through Eq. 7.28
2. **Φ_{multi} foundation:** Multi-physics Hamiltonian enables correlated measurements
3. **Γ_{mm} contributors:** Material quality factors (Table 7.11) impact model-mismatch
4. **Forward model basis:** Each sensing channel has defined \mathbf{G} operator (Eqs. 7.46–7.48)
5. **Array engineering:** 1D/2D/2.5D/3D configurations enable application-specific optimization
6. **Lattice matching:** Connection to Chapter 3 optical systems through Eq. 7.69
7. **Tomographic reconstruction:** 3D arrays improve Γ_{inv} through multi-plane constraints (connects to Chapter 14)
8. **Super-resolution modes:** CSD, STORM-NV, Spin-RESOLFT extend resolution below diffraction limit
9. **Hybrid workflow:** Screening + zoom strategy balances throughput and resolution

Problems and Solution Hints

Problem 7.1: Hamiltonian Eigenvalues

Derive the eigenvalues of the NV Hamiltonian in the presence of an axial magnetic field B_z and transverse strain E . Show that the transition frequencies are:

$$\nu_{\pm} = D \pm \sqrt{(\gamma_{\text{NV}} B_z)^2 + E^2} \quad (7.90)$$

Hint: Write the Hamiltonian in matrix form using the $|m_s\rangle$ basis and diagonalize. The 3×3 matrix block-diagonalizes into 1×1 ($|0\rangle$) and 2×2 ($|\pm 1\rangle$) blocks.

Problem 7.2: Sensitivity Optimization

An NV ensemble has $\Gamma = 5$ MHz, $C_0 = 0.25$, and $R = 10^6$ photons/s. Calculate:

- (a) The shot-noise limited sensitivity
- (b) The optimal Rabi frequency for maximum sensitivity
- (c) The sensitivity degradation if MW power is $10\times$ optimal

Hint: For (c), use the power-broadened contrast formula and note that linewidth also increases with power.

Problem 7.3: Multi-Physics Channel Separation

An ODMR measurement yields $\nu_+ = 2.905$ GHz and $\nu_- = 2.835$ GHz.

- (a) Extract the magnetic field B_z
- (b) Extract the temperature shift ΔT from room temperature
- (c) If the temperature measurement has ± 5 K uncertainty, what is the uncertainty in B_z ?

Hint: The temperature uncertainty propagates to B_z through the common-mode shift.

Problem 7.4: Ensemble Scaling

Design an NV ensemble to achieve $1 \text{ nT}/\sqrt{\text{Hz}}$ sensitivity with:

- (a) Maximum density (what limits apply?)
- (b) Minimum NV count if single-NV sensitivity is $10 \mu\text{T}/\sqrt{\text{Hz}}$
- (c) Required layer thickness for 10^8 NV in a $100 \mu\text{m} \times 100 \mu\text{m}$ area

Hint: Check against dipolar broadening limit and nitrogen aggregation threshold.

Problem 7.5: Charge State Dynamics

Under 532 nm excitation at 50 kW/cm^2 , steady-state NV^- fraction is 60%. The conversion rates are $k_+ = 0.1 \text{ ms}^{-1}$ (NV^- to NV^0) at this power.

- (a) Calculate k_- (NV^0 to NV^-)
- (b) How long after excitation turn-on does the system reach 90% of steady state?
- (c) Design a repump protocol using 590-nm light to maintain >80% NV^- fraction

Hint: The time constant is $\tau = 1/(k_+ + k_-)$. For (c), model the repump as increasing k_- by a factor proportional to repump intensity.

Problem 7.6: Engineered Array Design

Design a 2D NV array for imaging TSV (through-silicon via) defects at 50 μm depth.

- (a) Given single-NV sensitivity $\eta_B^{\text{single}} = 1 \mu\text{T}/\sqrt{\text{Hz}}$, calculate the required areal NV density for 10 nT/ $\sqrt{\text{Hz}}$ per 2 μm pixel
- (b) Determine if this density exceeds the dipolar interaction limit ($d_{\min} = 15 \text{ nm}$)
- (c) Propose a multi-layer 3D array configuration to improve depth disambiguation. Specify layer depths and the expected improvement in depth resolution

Hint: For (a), use Eq. 7.53. For (c), consider that multiple sensing planes at different depths provide independent measurements of the field decay profile.

Problem 7.7: Lattice-Matched Optical Addressing

An optical lattice for parallel NV excitation uses 532 nm light with symmetric 60° beam crossing.

- (a) Calculate the lattice period in diamond ($n = 2.42$)
- (b) Design an NV array with pitch matching this lattice period
- (c) If fabrication tolerance is $\pm 5 \text{ nm}$ on the NV pitch, calculate the resulting excitation efficiency variation across a $100 \times 100 \mu\text{m}^2$ field

Hint: For (c), the efficiency varies as $\cos^2(\Delta k \cdot L/2)$ where Δk is the lattice mismatch and L is the array size.

Problem 7.8: 3D Tomographic Array Design

Design a 3D NV array for depth-resolved current imaging with sources spanning 5–40 μm depth.

- (a) Using the geometric progression rule (Theorem 7.8.2), determine optimal layer positions for $N_z = 4$ layers
- (b) Calculate the expected improvement in Γ_{inv} compared to a single 2D layer, assuming $\kappa_0 = 150$ and $\text{SNR} = 80$
- (c) Estimate the depth resolution achievable with this configuration
- (d) How would adding thermal sensing (multi-physics) improve depth disambiguation?

Hint: For (a), use $z_1 = 0.5 \mu\text{m}$ (practical minimum). For (d), consider that thermal diffusion provides an independent depth signature with characteristic length $L_{\text{thermal}} = \sqrt{\alpha/\pi f}$.

Problem 7.9: CSD Super-Resolution Design

Design a CSD microscopy system to achieve 25 nm resolution for single-defect characterization.

- (a) Calculate the required depletion intensity ratio $I_{\text{max}}/I_{\text{sat}}$
- (b) For $I_{\text{sat}} = 50 \text{ kW/cm}^2$, what laser power is needed for a 1 μm diameter donut beam?
- (c) Estimate the acquisition time per point if 1000 photons are needed for adequate SNR and the count rate is 100 kcps
- (d) What is the maximum scan area achievable in 1 hour?

Hint: The donut beam peak intensity is approximately $4P/(\pi w^2)$ where w is the beam radius.

Problem 7.10: Alternative Color Center Selection

Compare NV⁻ and SiV⁻ centers for a strain imaging application requiring:

- Strain sensitivity: 100 kPa/ $\sqrt{\text{Hz}}$
- Temperature: 300 K (room temperature)
- Spatial resolution: 500 nm

- (a) Calculate the required ODMR linewidth for each center type
- (b) Which center type is preferred and why?
- (c) Design a hybrid array using both NV and SiV for optimal B, T, and σ sensing

Hint: SiV has much higher strain sensitivity but limited T_2 at room temperature. Consider using SiV for strain reference and NV for magnetic sensing.

References

- [7.1] M. W. Doherty, N. B. Manson, P. Delaney, F. Jelezko, J. Wrachtrup, and L. C. L. Hollenberg, “The nitrogen-vacancy colour centre in diamond,” *Physics Reports*, vol. 528, no. 1, pp. 1–45, 2013.
- [7.2] L. Rondin, J.-P. Tetienne, T. Hingant, J.-F. Roch, P. Maletinsky, and V. Jacques, “Magnetometry with nitrogen-vacancy defects in diamond,” *Reports on Progress in Physics*, vol. 77, no. 5, p. 056503, 2014.
- [7.3] J. F. Barry, J. M. Schloss, E. Bauch, M. J. Turner, C. A. Hart, L. M. Pham, and R. L. Walsworth, “Sensitivity optimization for NV-diamond magnetometry,” *Reviews of Modern Physics*, vol. 92, no. 1, p. 015004, 2020.
- [7.4] F. Dolde, H. Fedder, M. W. Doherty, T. Nöbauer, F. Rempp, G. Balasubramanian, T. Wolf, F. Reinhard, L. C. L. Hollenberg, F. Jelezko, and J. Wrachtrup, “Electric-field sensing using single diamond spins,” *Nature Physics*, vol. 7, no. 6, pp. 459–463, 2011.
- [7.5] V. M. Acosta, E. Bauch, M. P. Ledbetter, A. Waxman, L.-S. Bouchard, and D. Budker, “Temperature dependence of the nitrogen-vacancy magnetic resonance in diamond,” *Physical Review Letters*, vol. 104, no. 7, p. 070801, 2010.
- [7.6] G. Balasubramanian, I. Y. Chan, R. Kolesov, M. Al-Hmoud, J. Tisler, C. Shin, C. Kim, A. Wojcik, P. R. Hemmer, A. Krueger, T. Hanke, A. Leitenstorfer, R. Bratschitsch, F. Jelezko, and J. Wrachtrup, “Nanoscale imaging magnetometry with diamond spins under ambient conditions,” *Nature*, vol. 455, no. 7213, pp. 648–651, 2008.
- [7.7] D. Le Sage, K. Arai, D. R. Glenn, S. J. DeVience, L. M. Pham, L. Rahn-Lee, M. D. Lukin, A. Yacoby, A. Komeili, and R. L. Walsworth, “Optical magnetic imaging of living cells,” *Nature*, vol. 496, no. 7446, pp. 486–489, 2013.
- [7.8] J.-P. Tetienne, T. Hingant, L. Rondin, A. Cavaillès, L. Mayer, G. Dantelle, T. Gacoin, J. Wrachtrup, J.-F. Roch, and V. Jacques, “Spin relaxometry of single nitrogen-vacancy defects in diamond nanocrystals for magnetic noise sensing,” *Physical Review B*, vol. 87, no. 23, p. 235436, 2013.
- [7.9] E. D. Herbschleb, H. Kato, Y. Maruyama, T. Danjo, T. Makino, S. Yamasaki, I. Ohki, K. Hayashi, H. Morishita, M. Fujiwara, and N. Mizuochi, “Ultra-long coherence times amongst room-temperature solid-state spins,” *Nature Communications*, vol. 10, no. 1, p. 3766, 2019.
- [7.10] A. Nowodzinski, M. Chipaux, L. Toraille, V. Jacques, J.-F. Roch, and T. Debuisschert, “Nitrogen-Vacancy centers in diamond for current imaging at the redistributive layer level of Integrated Circuits,” *Microelectronics Reliability*, vol. 55, no. 9-10, pp. 1549–1553, 2015.
- [7.11] C. Hepp, T. Müller, V. Waselowski, J. N. Becker, B. Pingault, H. Sternschulte, D. Steinmüller-Nethl, A. Gali, J. R. Maze, M. Atatüre, and C. Becher, “Electronic structure of the silicon vacancy color center in diamond,” *Physical Review Letters*, vol. 112, no. 3, p. 036405, 2014.
- [7.12] M. K. Bhaskar, D. D. Sukachev, A. Sipahigil, R. E. Evans, M. J. Burek, C. T. Nguyen, L. J. Rogers, P. Siyushev, M. H. Metsch, H. Park, F. Jelezko, M. Lončar, and M. D. Lukin, “Quantum nonlinear optics with a germanium-vacancy color center in a nanoscale diamond waveguide,” *Physical Review Letters*, vol. 118, no. 22, p. 223603, 2017.
- [7.13] E. Rittweger, K. Y. Han, S. E. Irvine, C. Eggeling, and S. W. Hell, “STED microscopy reveals crystal colour centres with nanometric resolution,” *Nature Photonics*, vol. 3, no. 3, pp. 144–147, 2009.

- [7.14] P. C. Maurer, J. R. Maze, P. L. Stanwix, L. Jiang, A. V. Gorshkov, A. A. Zibrov, B. Harke, J. S. Hodges, A. S. Zibrov, A. Yacoby, D. Twitchen, S. W. Hell, R. L. Walsworth, and M. D. Lukin, “Far-field optical imaging and manipulation of individual spins with nanoscale resolution,” *Nature Physics*, vol. 6, no. 11, pp. 912–918, 2010.
- [7.15] A. Gruber, A. Dräbenstedt, C. Tietz, L. Fleury, J. Wrachtrup, and C. von Borczyskowski, “Scanning confocal optical microscopy and magnetic resonance on single defect centers,” *Science*, vol. 276, no. 5321, pp. 2012–2014, 1997.